

Link prediction with hyperbolic geometry

Maksim Kitsak,^{1,2} Ivan Voitalov,^{1,2} and Dmitri Krioukov^{3,2}

¹*Department of Physics, Northeastern University, 110 Forsyth Street,
111 Dana Research Center, Boston, MA 02115, USA.*

²*Network Science Institute, Northeastern University, 177 Huntington Avenue, Boston, MA, 02215*

³*Department of Physics, Department of Mathematics,
Department of Electrical & Computer Engineering, Northeastern University,
110 Forsyth Street, 111 Dana Research Center, Boston, MA 02115, USA.*

(Dated: June 11, 2022)

Link prediction is a paradigmatic problem in network science with a variety of applications. In latent space network models this problem boils down to ranking pairs of nodes in the order of increasing latent distances between them. The network model with hyperbolic latent spaces has a number of attractive properties suggesting it must be a powerful tool to predict links, but the past work in this direction reported mixed results. Here we perform systematic investigation of the utility of latent hyperbolic geometry for link prediction in networks. We first show that some measures of link prediction accuracy are extremely sensitive with respect to inaccuracies in the inference of latent hyperbolic coordinates of nodes, so that we develop a new coordinate inference method that maximizes the accuracy of such inference. Applying this method to synthetic and real networks, we then find that while there exists a multitude of competitive methods to predict obvious easy-to-predict links, among which hyperbolic link prediction is rarely the best but often competitive, it is the best, often by far, when the task is to predict less obvious missing links that are really hard to predict. These links include missing links in incomplete networks with large fractions of missing links, missing links between nodes that do not have any common neighbors, and missing links between dissimilar nodes at large latent distances. Overall these results suggest that the harder a specific link prediction task is, the more seriously one should consider using hyperbolic geometry.

I. INTRODUCTION

Link prediction is a paradigmatic example of forecasting network dynamics [1–4], with diverse applications including the reconstruction of networks based on partial data [5, 6] and prediction of future social ties [1, 7, 8], protein interactions [9–11], and user ratings in recommender systems [12–15].

Latent space network models [16–20] offer an intuitive and simple approach to link prediction. In these models, network nodes are points in a latent space, while connections are established with probabilities that decrease with latent distances between nodes. Latent distances model similarity between nodes, and the main idea behind these models is to model homophily: more similar nodes are more likely to be linked. Link prediction then reduces to ranking unconnected node pairs in the order of increasing latent distances between them: the closer the two unlinked nodes in the latent space, the higher the probability of a missing link [4, 21–23].

Among many latent space models considered in literature, only the one that assumes that the latent space is hyperbolic, reproduces sparsity, self-similarity, scale-free degree distribution, strong clustering, the small-world property, and community structure [19, 24–26]. All these properties are often observed in many real networks [27–29], and hyperbolic geometry captures them all. In addition, the hyperbolic network model is likely to be the simplest or parsimonious with respect to these properties, as in some of its limiting regimes it has been proven to be statistically unbiased, satisfying the maximum en-

tropy principle [30, 31].

Given the combination of these attractive properties, one could naturally expect that the hyperbolic latent space model must be a powerful tool in link prediction. Yet the previous studies on this subject reported mixed results [23, 32–36].

Here we perform systematic investigation of the efficiency of link prediction using latent hyperbolic geometry. In Section II, we first recall the definitions of the hyperbolic latent space network model, which for short we call hyperbolic random graphs (HRGs), and of the main measures of link prediction accuracy: AUC (Area under Receiver-Operating Characteristic), AUPR (Area under Precision-Recall Curve), and Precision. We also discuss there what the AUC and AUPR measures actually measure: while AUPR cares mostly about most obvious easy-to-predict missing links, AUC puts more weight on less obvious and harder-to-predict missing links between more dissimilar nodes at large latent distances, albeit with the cost of not caring that much about false positives. Our main results are then in Sections III and IV:

Section III: Upper bounds of link predictability with hyperbolic geometry. Here we calculate analytically the AUC and AUPR on HRGs with *known* hyperbolic coordinates of all nodes. That is, the same coordinates are used both to generate HRGs and to predict missing links in them, an ideal situation yielding the upper bound for the link prediction accuracy using hyperbolic geometry. To understand the robustness of link prediction in the case where coordinates are inferred (Section IV), so that they are not equal exactly to the true coordinates, we add uniform noise to the true coor-

ordinates, and analyze the AUC, AUPR, and Precision as functions of the noise amplitude to find that:

- AUC is not that sensitive to noise, but
- AUPR and Precision decrease quickly as noise grows.

The latter result implies that the AUPR and Precision scores of link prediction using hyperbolic geometry in real networks can be high only if node coordinates are inferred with sufficiently high accuracy. This is because the most likely missing links candidates are those between similar nodes at small hyperbolic distances, which are most sensitive to coordinate inaccuracies.

Section IV: Link prediction in real networks and HRGs with *inferred* coordinates. To predict missing links in networks with unknown coordinates one first needs to infer these coordinates. Motivated by the results in Section III calling for high-accuracy coordinate inference, and given that no existing hyperbolic coordinate inference algorithm is sufficiently accurate, we develop a new one, which we call *HyperLink Embedder*, whose focus is on high precision in coordinate inference. We describe it in Appendix E, where we also compare it to some existing inference algorithms to show that its accuracy is indeed higher. We then apply it to a collection of HRGs with “forgotten” coordinates, and to real networks, calling the overall link prediction procedure as the *HyperLink* method. Comparing the HyperLink to a representative collection of other link prediction methods, we find that:

- HyperLink’s AUC scores are always the best.
- HyperLink’s AUPR and Precision scores in
 - HRGs: the best if, surprisingly, clustering is weak, and/or the degree distribution exponent γ is high,
 - real networks: the scores are rarely the best but are often competitive, especially if the fraction of missing links is high.
- In prediction of nonlocal links, which are links between nodes that do not have any common neighbors (such links are really hard to predict, and tend to comprise significant fractions of all missing links), the HyperLink is always by far the best, according to all the AUC, AUPR, and Precision measures.

In Section V we conclude the paper with a more detailed summary of these results, their discussion, and an outline of open problems.

II. METHODS

We begin the exposition by discussing the latent-geometric link prediction framework and the null model that we utilize to predict missing links.

A. Link prediction with latent geometry

Link prediction with hyperbolic geometry is a two-step procedure. First, one needs to infer node coordinates in the hyperbolic space and calculate hyperbolic distances between node pairs. This coordinate inference procedure is often referred to as network mapping or embedding. The second step of the procedure is to identify most likely missing link candidates. This subsection focuses on the second step of this procedure, while the technical details of the null geometric model and the network mapping algorithm constituting the first step, are provided, respectively, in Section II B and Appendix (E). We refer to the network mapping algorithm and the entire hyperbolic link prediction framework as the *HyperLink Embedder* and the *HyperLink*, respectively.

The latent-geometric link prediction framework is applicable to all latent geometric models, where connections are established independently with decreasing connection probability function $p(x)$. Intuitively, the smaller the latent distance between two nodes, the higher the probability of a link between them. Then, if two nodes located close to each other in the latent space are not connected, it is likely that there is a missing link between them.

Specifically, consider a latent-geometric model where nodes are assigned positions $\{\mathbf{x}_i\}$ in a certain latent space \mathcal{M} , and every node pair $\{ij\}$ is connected with probability $p_{ij} = p(x_{ij})$, where $x_{ij} = d(\mathbf{x}_i, \mathbf{x}_j)$ is the latent distance between the nodes, and $p : \mathbb{R}_+ \rightarrow [0, 1]$ is the decreasing connection probability function specified by the model. After all connections are established, some links are removed with probabilities $1 - q_{ij}$. These pairs of nodes are referred to as missing links.

Any unconnected node pair $\{ij\}$ in the resulting network is either not connected in the network formation process, or connected in the network formation and later removed with probability $1 - q_{ij}$. Therefore, the probability for an unconnected pair of nodes $\{ij\}$ separated by x_{ij} to be a missing link, is

$$\tilde{p}(x_{ij}) = \frac{p(x_{ij})(1 - q_{ij})}{1 - p(x_{ij}) + p(x_{ij})(1 - q_{ij})}. \quad (1)$$

In the particular case of a decreasing connection probability function $p(x)$ and the random link removal process, $q_{ij} = q$

$$\tilde{p}(x_{ij}) = \frac{(1 - q)p(x_{ij})}{1 - qp(x_{ij})} \quad (2)$$

is the decreasing function of x_{ij} for any $q > 0$. Thus, the most probable candidates for missing links are indeed unconnected node pairs located at small latent distances, as stated, and the latent-geometric link prediction algorithm only needs to rank unconnected node pairs in the increasing order of latent distance between them.

It is important to note, however, that this approach is only guaranteed to work in the case the links are removed uniformly at random. In the general case, missing link

probabilities in Eq. (1) depend both on latent distances $\{x_{ij}\}$ and missing link rates $\{1 - q_{ij}\}$ and further information on the nature of $\{q_{ij}\}$ is needed to rank missing link candidates properly.

B. Hyperbolic Random Graphs

While the latent-geometric framework described above is applicable to all latent-space models, in our work we use the HRG model as a null model for link prediction.

HRGs have been extensively studied in the literature [19, 33, 34, 37–41] and have been shown to reproduce common properties of many real networks including heterogeneous distributions of node degrees, strong clustering, as well as community structure [19, 26, 42].

The latent space of the HRG model is the two-dimensional hyperbolic disk of constant negative curvature $K = -1$ and radius R . The hyperbolic distance x between any two points in the hyperbolic disk is given by the hyperbolic law of cosines:

$$\cosh x = \cosh r \cosh r' - \sinh r \sinh r' \cos \Delta\theta, \quad (3)$$

where (r, θ) and (r', θ') are the hyperbolic coordinates of the two points within the disk and $\Delta\theta = \pi - |\pi - |\theta - \theta'|||$ is the angle between them.

The HRG model has three parameters — hyperbolic disk radius $R > 0$, temperature $T \in [0, 1)$ and node density parameter $\alpha > 1/2$ - and is defined as follows:

1. Draw node coordinates $\{r_i, \theta_i\}$, $i = 1, \dots, N$, from pdfs:

$$\theta_i \sim \rho(\theta) = 1/(2\pi), \quad \theta_i \in [0, 2\pi], \quad (4)$$

$$r_i \sim \rho(r) = \frac{\sinh(\alpha r)}{\cosh(\alpha R) - 1}, \quad r_i \in [0, R] \quad (5)$$

2. Compute distances $\{x_{ij}\}$ between all node pairs using Eq. (3).
3. Connect node pairs with probability

$$p(x_{ij}) = \frac{1}{1 + e^{-\frac{x_{ij} - R}{2T}}}. \quad (6)$$

We summarize basic HRG properties in Appendices C: parameter α controls the exponent $\gamma = 2\alpha + 1$ of the power-law degree distribution, while clustering is a decreasing function of temperature T approaching 0 in the $N \rightarrow \infty$ limit as $T \rightarrow 1$. In this limit, clustering is zero for any $T \geq 1$.

C. Link Prediction Accuracy

We evaluate the accuracy of the HyperLink as well as other link prediction methods through random link removal experiments. To this end, we first remove existing

links uniformly at random with probability $1 - q$ from the network of interest G . We refer to the remaining network as *pruned* network and denote it by \tilde{G} . We refer to removed links as missing links and denote them by Ω_R . The set of remaining links in \tilde{G} is referred to as Ω_E .

To test the link prediction method of interest we compute likelihood scores for all unconnected node pairs in \tilde{G} , $\bar{\Omega}_E$, which include both missing links Ω_R and true non-links Ω_N , so that $\bar{\Omega}_E = \Omega_R \cup \Omega_N$. We then rely on these scores to rank unconnected node pairs in the decreasing order of missing link likelihood and refer to them as missing link candidates. We denote the fraction of $\lambda \in [0, 1]$ of most likely missing link candidates as set $\Omega_M(\lambda)$. In the case $\lambda = 0$, $\Omega_M(\lambda)$ is the empty set, while in the $\lambda = 1$ case $\Omega_M(\lambda) = \Omega_R \cup \Omega_N = \bar{\Omega}_E$.

In the case the exact number of missing links is known, the most direct way to assess link prediction accuracy is to consider the same number of the most likely missing link candidates and evaluate its intersection with the set of missing links. This metric is known as Precision and is formally defined as

$$\text{Precision} = \frac{|\Omega_R \cap \Omega_M(\lambda^*)|}{|\Omega_R|}, \quad (7)$$

where fraction $\lambda^* = 1 - q$ is chosen such that $|\Omega_M(\lambda^*)| = |\Omega_R|$. The Precision score is bounded by 0 and 1 with the upper bound corresponding to the ideal link predictor ranking all missing links in Ω_R higher than non-links in Ω_N .

In practical circumstances, however, the exact number of missing links is often unknown. Further, depending on the application, one might be interested to minimize the number of false positives in the prediction set, possibly by the expense of false negatives, or vice versa, minimize the number of false negatives by the expense of false positives. One example of the former case where one is interested to minimize the number of false positives, i.e., good citizens misclassified as criminals, is the criminal justice system. This example is in contrast to cancer screening, where the number of false negatives, or not-identified cancer cases, should be minimized. In both cases one is interested to explore the performance of the link predictor for a range of $\Omega_M(\lambda)$ sizes.

A number of link prediction metrics has been developed to this end with the Receiver Operating Characteristic (ROC) and the Precision-Recall (PR) being the most popular.

To formally introduce ROC and PR curves we first define the confusion matrix. The latter consists of four values, the numbers of *true positives* (TP), *false positives* (FP), *false negatives* (FN), and *true negatives* (TN), Fig. 1, and is extensively used in statistical classification problems. Link prediction is not a genuine classification problem since one is only interested to predict links and not their absence. Non-link node pairs are predicted implicitly as unconnected node pairs that are not part of Ω_R .

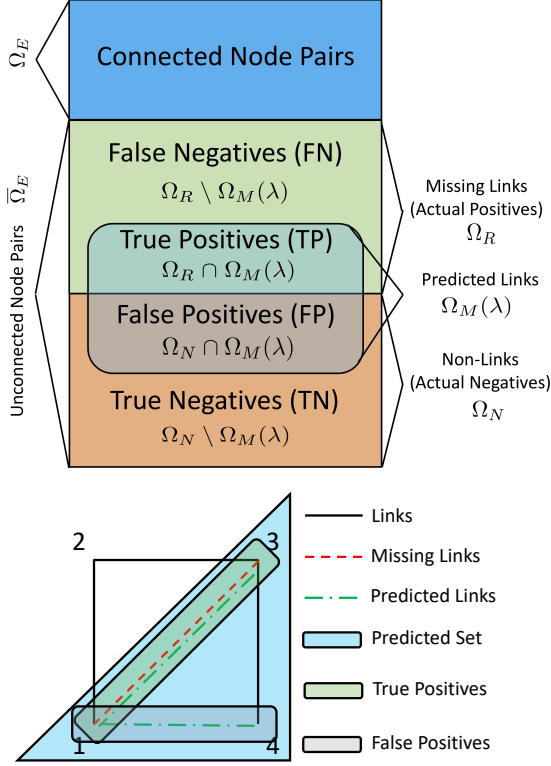


FIG. 1: **Confusion matrix and a toy example of link prediction.** (Top) Confusion matrix for link prediction. (Bottom) Toy link prediction example. Existing links are shown with solid black lines. Missing links, $\Omega_R = \{13\}$, are shown with red dotted lines, while predicted missing links, $\Omega(\lambda) = \{13, 14\}$ are shown with green dashed lines. In this example the sizes of the confusion matrix sets are $TP = 1$, $FP = 1$, $FN = 0$, and $TN = 1$.

In the context of link prediction, the number of true positives is the number of correctly identified missing links from $\Omega_M(\lambda)$, Eq. (8). The number of false negatives is the remaining number of missing links that are not part of the $\Omega_M(\lambda)$, Eq. (9). The number of false positives is the number of missing link candidates in $\Omega_M(\lambda)$ that are not correctly identified, Eq. (10). Finally, the number of true negatives is the number of unconnected node pairs that are neither true positives, nor false positives nor false negatives, see Eq. (11) and Fig. 1.

$$TP(\lambda) = |\Omega_R \cap \Omega_M(\lambda)|, \quad (8)$$

$$FN(\lambda) = |\Omega_R \setminus \Omega_M(\lambda)|, \quad (9)$$

$$FP(\lambda) = |\Omega_N \cap \Omega_M(\lambda)|, \quad (10)$$

$$TN(\lambda) = |\Omega_N \setminus \Omega_M(\lambda)|. \quad (11)$$

Since network sizes vary, it is common to normalize confusion matrix elements, obtaining true positive, false positive, false negative and true negative rates, formally

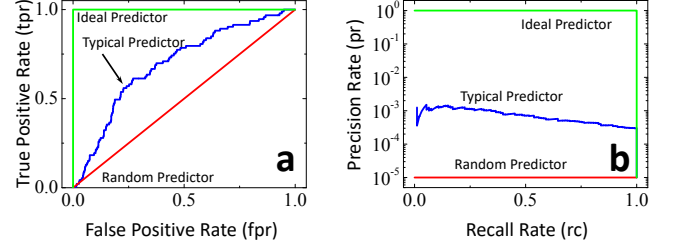


FIG. 2: Sketches of typical, **a**, ROC and, **b**, PR curves.

defined as:

$$tpr(\lambda) \equiv \frac{TP(\lambda)}{|\Omega_R|}, \quad (12)$$

$$fnr(\lambda) \equiv \frac{FN(\lambda)}{|\Omega_R|}, \quad (13)$$

$$fpr(\lambda) \equiv \frac{FP(\lambda)}{|\Omega_N|}, \quad (14)$$

$$tnr(\lambda) \equiv \frac{TN(\lambda)}{|\Omega_N|}, \quad (15)$$

$$(16)$$

ROC statistics or curve is defined as the parametric plot of the true positive rate $tpr(\lambda)$ as function of the false positive rate $fpr(\lambda)$ obtained by varying the fraction of considered link candidates $\lambda \in [0, 1]$. The ideal predictor is expected to rank all node pairs corresponding to missing links, Ω_R , higher than non-links, Ω_N , resulting in unit true positive rate and zero false positive rate for $\lambda = 1 - q$, $tpr(1 - q) = 1$, $fpr(1 - q) = 0$. The corresponding ROC curve of the ideal predictor is thus a rectangle going through the upper left corner $(0, 1)$ of the ROC space. A fully random link predictor, on the other hand, will guess missing links at random from $\bar{\Omega}_E$ and is expected to yield equal true positive and false positive rates, $tpr(\lambda) = fpr(\lambda)$ for all λ values, resulting in the diagonal ROC curve, Fig. 2a.

The standard way to quantify ROC-based prediction accuracy is through the Area under ROC curve (AUC),

$$AUC = \int_0^1 tpr(\lambda) fpr'(\lambda) d\lambda. \quad (17)$$

AUC values vary in between 0 and 1 with $AUC = 0.5$ corresponding to fully random predictor and $AUC = 1.0$ corresponding to the perfect predictor.

The AUC score can be interpreted as the probability that a randomly chosen missing link is assigned a higher link prediction score than a randomly chosen unconnected node pair. ROC curves are easy to read and interpret, which is arguably the basic reason behind their popularity.

At the same time, there is a growing consensus that ROC curves and corresponding AUC scores are insensitive in class imbalance problems, where the size of the

positives is disproportional to that of the negatives [43]. Link prediction in sparse networks is one example of class imbalance. Here the number of missing links is of the order of N and is significantly smaller than the number non-links which is of the order of N^2 . Intuitively, in this situation $\text{tpr}(\lambda)$ rate grows much faster than false positive rate since the latter is normalized by $|\Omega_N|$ and, as a result, most ROC curves tend to be substantially above the random baseline, yielding AUC scores close to 1.0, regardless of the link prediction method.

An alternative to the ROC curve is the PR characteristic, defined as the parametric plot of the precision rate $\text{pr}(\lambda)$ as a function of the recall rate $\text{rc}(\lambda)$ obtained by varying $\lambda \in [0, 1]$, where the two rates are defined by

$$\text{pr}(\lambda) \equiv \frac{\text{TP}(\lambda)}{|\Omega_M(\lambda)|}, \quad (18)$$

$$\text{rc}(\lambda) \equiv \frac{\text{TP}(\lambda)}{|\Omega_R|} = \text{tpr}(\lambda). \quad (19)$$

That is, the recall rate is identical to the true positive rate, while the precision rate differs from the latter by a different normalization - to the number of predicted links versus the number of removed links.

In the case of ideal predictor precision rate is maximized, $\text{pr}(\lambda) = 1.0$ for $\lambda \leq 1 - q$, while the recall is growing from $\text{rc}(0) = 0$ to $\text{rc}(1 - q) = 1$, resulting in the rectangular PR curve going through the upper right corner (1, 1) of the PR space. A fully random predictor, on the other hand, maintains constant precision rate equal to the ratio of the number of true missing links to the total number of unconnected node pairs, $\text{pr}^{\text{rand}}(\lambda) = \frac{|\Omega_R|}{|\Omega_R| + |\Omega_N|}$ for all λ values, Fig. 2b. The standard metric quantifying PR-based prediction accuracy is the Area under PR curve (AUPR),

$$\text{AUPR} = \int_0^1 \text{pr}(\lambda) \text{rc}'(\lambda) d\lambda. \quad (20)$$

AUPR values vary between $\frac{|\Omega_R|}{|\Omega_R| + |\Omega_N|}$ and 1 with the unit score corresponding to the ideal predictor. In the case of sparse networks $\Omega_R \ll \Omega_N$, leading to $\text{AUPR} \ll 1$ in the case of a random predictor. Unlike ROC curves, PR characteristics does not directly depend on the number of true negatives and, as a result, does not suffer from the class imbalance problem in case of sparse networks.

D. AUC versus AUPR

While both AUC and AUPR quantify link prediction accuracy, they tend to weigh missing link candidates differently. AUPR scores tends to emphasize highly ranked missing links candidates, i.e., those corresponding to small λ values. AUC scores, on the other hand, put more weight on missing links candidates corresponding to larger λ values.

Indeed, AUPR averages precision rate $\text{pr}(\lambda)$ over the recall rate $\text{rc}(\lambda)$. Since the recall rate is given by $\text{rc}(\lambda) = \frac{|\Omega_R \cap \Omega_M(\lambda)|}{|\Omega_R|}$, Eq. (19), good link predictors tend to reach $\text{rc}(\lambda) = 1$ values when the size of missing link candidates set $\Omega_M(\lambda)$ becomes comparable to that of Ω_R : $|\Omega_M(\lambda)| \sim |\Omega_R| \ll |\Omega_N|$. The latter inequality holds in the case of sparse networks, where the number of links is much smaller than the number of non-links. Thus, $|\Omega_M(\lambda)| \ll |\Omega_N|$, which corresponds to $\lambda \ll 1$ values. Thus, AUPR link prediction scores are dominated by small λ fractions, i.e., by the most likely and, typically, most obvious missing link candidates in Ω_M .

AUC scores, on the other hand, average true positive rate $\text{tpr}(\lambda)$ over false positive rate $\text{fpr}(\lambda)$. The latter takes large values when $|\Omega_M(\lambda)|$ becomes comparable to $|\Omega_N|$, i.e. for λ values close to 1. AUC scores, thus, are emphasizing not only easy-to-predict links at small λ values but also harder to predict links in Ω_M at intermediate and large λ values.

In summary, AUC and AUPR scores complement each other by weighing missing link candidates in Ω_M differently. Thus, in our work we compute both metrics to obtain a comprehensive view on the utility of hyperbolic geometry in link prediction. In addition to AUPR and AUC scores, we also compute Precision scores, which are the scores to use if the number of missing links is known exactly, although such knowledge is rarely the case in practice.

III. LINK PREDICTION WITH KNOWN COORDINATES

Before investigating link prediction accuracy in real networks, we conduct link prediction experiments on HRG graphs with known coordinates. In doing so we pursue several goals. The HRGs provide the upper bound for link prediction accuracy of the HyperLink if same node coordinates are used both for the construction of the graphs and for link prediction [23]. Thus, we want to quantify the upper bound of link predictability on HRG graphs. Second, we want to measure link prediction accuracies of other methods, listed in Appendix B, and compare them to that of the HyperLink. Establishing these results provides a baseline for interpreting link prediction results on real networks.

We start with the analysis of HyperLink accuracy in the case of randomly missing links in HRGs. After the generation of an HRG graph we visit each of its links and remove it with probability $1 - q$, arriving at pruned network. We then rank missing link candidates using distances between all unconnected node pairs calculated with coordinates from which the network was originally generated.

As seen in Fig. 3, the predictive power of the HyperLink is maximized as $T \rightarrow 0$ and decreases as T increases. This result is expected. In the $T \rightarrow 0$ limit the HRG model is deterministic since the connection prob-

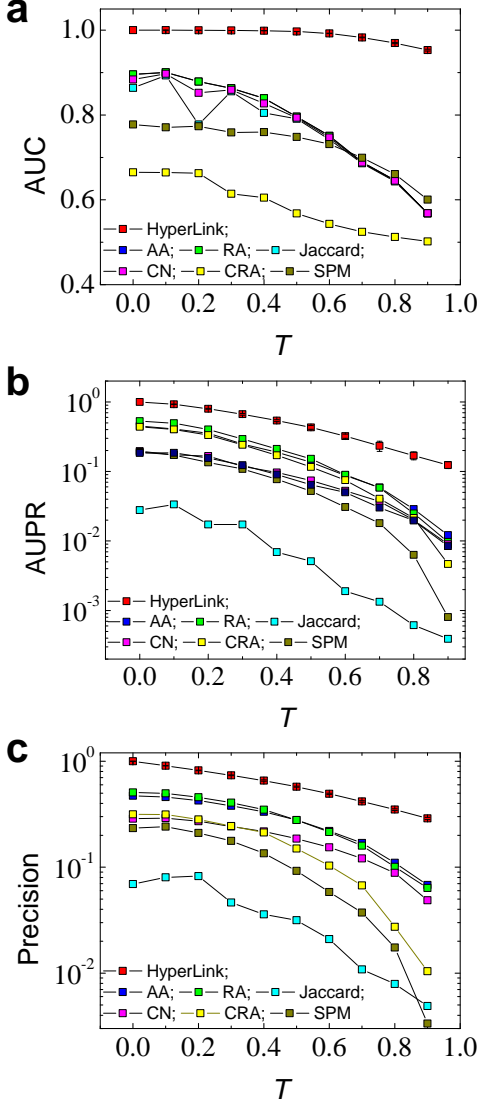


FIG. 3: **Link prediction on HRGs with known coordinates.** In all experiments we remove links uniformly at random with probability $1-q = 0.5$. Then missing links are predicted using hyperbolic distances between unconnected node pairs. Link prediction accuracy is quantified using, **a** AUC, **b** AUPR, and **c** Precision scores plotted as a function of HRG temperature T . All results correspond to HRG graphs with $N = 10^4$ nodes, $\gamma = 2.5$ and $\bar{k} = 10$. The HyperLink link prediction scores are compared to those of AA, RA, JC, CN, CRA, and SPM methods, see Appendix B.

ability in Eq. (6) becomes the Heaviside step function, $p(x) \rightarrow \Theta(R-x)$. As a result, all node pairs with $x < R$ are connected and other node pairs are not. Then, an unconnected pair of nodes at distance $x < R$ is guaranteed to be a true positive and all unconnected pairs at $x \geq R$ are true negatives. As T increases, connections are allowed at distances $x > R$ with increasing probability and, as a result, underlying geometry plays smaller role in the formation of links, explaining the decreasing link prediction accuracy as a function of T , as quantified by all scores in Fig. 3.

Even though all scores, AUC, AUPR and Precision, are decreasing functions of T , they behave differently. AUC scores remain constant in the $T \in (0, \frac{1}{2})$ interval and then exhibit a slow decay to AUC = 0.95 at $T = 0.9$. AUPR and Precision scores, on the other hand, decrease rapidly on the entire testing interval of $T \in [0, 0.9]$ from AUPR = 1 (Precision = 1) at $T = 0$ to AUPR = 0.34 (Precision = 0.29) at $T = 0.9$.

A. AUC

To understand the behavior of AUC scores as a function of HRG parameters we define distance-dependent true positive $\text{tpr}(x)$ and false positive $\text{fpr}(x)$ rates as the fractions of true and false positives, respectively, contained among unconnected node pairs separated by distances up to x .

$$\text{tpr}(x) = \frac{\text{tp}(x)}{(1-q)E} = \frac{1}{E} \binom{N}{2} \int_0^x n(y)p(y)dy, \quad (21)$$

$$\text{fpr}(x) = \frac{\binom{N}{2} \int_0^x n(y)(1-p(y))dy}{\binom{N}{2} - E}, \quad (22)$$

where E is the true number of links in the network, $E = |\Omega_E \cup \Omega_R|$, $p(y)$ is the connection probability in the HRG given by Eq. (6) and $n(y)$ is the distance distribution for node pairs in the HRG.

It is seen from Eqs. (21) and (22) that in the $T \rightarrow 0$ limit $p(y) = \Theta(R-y)$, resulting in $\text{fpr}(x) = 0$ for $x \leq R$ and $\text{tpr}(x) = 1$ for $x \geq R$, resulting in the ideal ROC curve, Fig. 2a, and AUC = 1.

To quantify the behavior of AUC in the $T > 0$ regime we rely on the functional form of $n(y)$, which has been found in [44]. It follows from Ref. [44] that $n(y)$ has the upper bound of

$$n(x) \leq \frac{4\alpha^2}{\pi(2\alpha-1)^2} e^{x/2-R}, \quad (23)$$

and this upper bound also provides its leading term behavior in the large N limit:

$$n(x) \sim \frac{4\alpha^2}{\pi(2\alpha-1)^2} e^{x/2-R}, \quad (24)$$

for $\alpha > \frac{1}{2}$.

Using Eq. (24), we can evaluate true and false positive rates, up to proportionality coefficient, as:

$$\text{tpr}(x) \sim \frac{4\alpha^2}{\pi(2\alpha-1)^2} \frac{N^2}{E} e^{-\frac{R}{2}} I\left(e^{\frac{x-R}{2}}; T\right), \quad (25)$$

$$\text{fpr}(x) \sim \frac{8\alpha^2}{\pi(2\alpha-1)^2} e^{-R} \left[e^{\frac{x}{2}} - e^{\frac{R}{2}} I\left(e^{\frac{x-R}{2}}; T\right) \right] \quad (26)$$

where

$$I(z; T) \equiv \int_0^z \frac{dx}{1+x^{1/T}} = z {}_2F_1\left(1, T, 1+T, -z^{1/T}\right), \quad (27)$$

and ${}_2F_1$ is the Gaussian Hypergeometric function. In the $z \ll 1$ regime $I(z; T) \approx z$ and, thus, $\text{tpr}(x) \approx e^{\frac{x-R}{2}}$ and $\text{fpr}(x) \approx 0$ for $x < R$, Fig. 4a,b.

This result is easy to interpret. Connection probability $p(x)$ is close to unity for $x < R$ and thus all unconnected node pairs with $x < R$ are almost guaranteed to be true positives, resulting in negligible false positive rates. Since missing links are removed uniformly at random, the number of true positives for $x < R$ grows proportional to the number of node pairs in the hyperbolic disk.

In the $z \gg 1$ regime $I(z; T) \sim I(T)$, where $I(T) = \frac{\pi}{T \sin(\pi/T)}$, explaining the saturation of the true positive rate, $\text{tpr}(x) \rightarrow 1$ as x approaches $2R$, and the exponential growth of the false positive rate, $\text{fpr}(x) \sim e^{\frac{x}{2}}$ for $x > R$, Fig. 4a,b.

The behavior of $\text{tpr}(x)$ and $\text{fpr}(x)$ provides a qualitative explanation for nearly perfect AUC scores observed in Fig. 3a. The false positive rate $\text{fpr}(x)$ takes large values only when x approaches $2R$. At the same time, as x approaches $2R$ the $\text{tpr}(x)$ approaches 1.

To obtain the analytical estimate of the AUC as a function of HRG parameters we represent it as

$$\text{AUC} = \int_0^{2R} \text{tpr}(x) \text{fpr}'(x) dx \quad (28)$$

By making use of Eqs. (21) and (22) we arrive at

$$\text{AUC} = 1 - \Delta_1 - \Delta_2, \quad (29)$$

$$\Delta_1 = \frac{E}{\binom{N}{2}}, \quad (30)$$

$$\Delta_2 = -\frac{1}{E} \binom{N}{2} \int_0^{2R} [n^c(x)]^2 p'(x) dx, \quad (31)$$

where $n^c(x) \equiv \int_0^x n(y) dy$.

In the case of sparse networks the first correction term $\Delta_1 \sim N^{-1}$ and can be ignored in the large N limit. The second correction term requires further analysis. It is straightforward to verify that in the $T \rightarrow 0$ limit $\Delta_2 \sim N^{-1}$ and can also be ignored. Indeed, in this case $p'(x) = -\delta(x - R)$, and

$$\Delta_2(T=0) = \frac{1}{E} \binom{N}{2} [n^c(R)]^2. \quad (32)$$

Since $\binom{N}{2} [n^c(R)]$ equals the number of node pairs in the hyperbolic disk with distances up to R and all these node pairs are connected in the $T \rightarrow 0$ case, $\binom{N}{2} [n^c(R)] = E$, resulting in $\Delta_2(T=0) = \frac{E}{\binom{N}{2}} \sim N^{-1}$.

To estimate the behavior of Δ_2 in the case of $T > 0$ we need to understand the behavior of its integrand in Eq. (31). Since $n^c(x) \sim e^{\frac{x}{2}}$ and $-p'(x) = \frac{1}{2T} \exp\left(\frac{x-R}{2T}\right) [p(x)]^2$, the integrand is sharply peaked at $x = R + 2T \ln\left(\frac{1+T}{1-T}\right)$ in the case of $T \in (0, \frac{1}{2})$, resulting in $\Delta_2 \sim N^{-1}$, similar to the $T \rightarrow 0$ case.

Conversely, the integrand in Eq. (31) grows monotonously as a function of x in the case of

$T \in (\frac{1}{2}, 1)$. The evaluation of Δ_2 in this regime is quite involved and is not informative. Instead, we elect to compute the upper bound for Δ_2 , which also provides the lower bound for AUC scores. In doing so we note that the leading term behavior of $n(x)$ given by Eq. (24) is also its upper bound, see Ref. [44]. Then

$$\Delta_2 \leq \frac{2\alpha^2 e^{-R} \binom{N}{2}}{\pi T (2\alpha - 1)^2 E} \int_0^{2R} \frac{e^{(x-R)(1+\frac{1}{2T})} dx}{\left[1 + e^{\frac{x-R}{2T}}\right]^2} \sim N^{1-\frac{1}{T}}, \quad (33)$$

since $e^{\frac{R}{2}} \sim N$ in the case of sparse HRGs, see Eq. (C3). In the case of $T = \frac{1}{2}$ Eq. (33) simplifies to

$$\Delta_2 \leq \frac{4\alpha^2 e^{-R} \binom{N}{2}}{\pi (2\alpha - 1)^2 E} \int_0^{2R} \frac{e^{2(x-R)} dx}{[1 + e^{x-R}]^2} \sim \frac{\ln N}{N}. \quad (34)$$

Taken together, the results above show that the AUC scores for HRG graphs with known coordinates converge to 1 in the large N limit as

$$1 - \text{AUC} \begin{cases} \sim N^{-1} & \text{if } T \in [0, \frac{1}{2}) , \\ \mathcal{O}\left(\frac{\ln N}{N}\right) & \text{if } T = \frac{1}{2} , \\ \mathcal{O}\left(N^{1-\frac{1}{T}}\right) & \text{if } T \in (\frac{1}{2}, 1) \end{cases} \quad (35)$$

B. AUPR

AUPR scores can be evaluated in a similar fashion:

$$\text{AUPR} = \int_0^{2R} \text{pr}(x) \text{rc}'(x) dx, \quad (36)$$

where $\text{pr}(x)$ and $\text{rc}(x)$ are, respectively, distance-dependent precision and recall functions for hyperbolic distances up to x :

$$\text{pr}(x) \equiv \frac{\text{tp}(x)}{N_d(x)}, \quad (37)$$

$$\text{rc}(x) \equiv \text{tpr}(x) = \frac{\text{tp}(x)}{(1-q)E}, \quad (38)$$

where $N_d(x)$ is the number of disconnected node pairs with distances up to x :

$$N_d(x) = \binom{N}{2} \int_0^x n(y) [1 - qp(y)] dy. \quad (39)$$

Using Eqs. (21) and (39) we obtain

$$\text{pr}(x) = (1-q) \frac{\int_0^x n(y) p(y) dy}{\int_0^x n(y) [1 - qp(y)] dy}, \quad (40)$$

$$\text{rc}(x) = \frac{1}{E} \binom{N}{2} \int_0^x n(y) p(y) dy. \quad (41)$$

In the $T \rightarrow 0$ limit $\text{pr}(x) = 1$ for all $x < R$, while $\text{rc}(x) = E(x)/E$, resulting, as expected, in $\text{AUPR} = 1$.

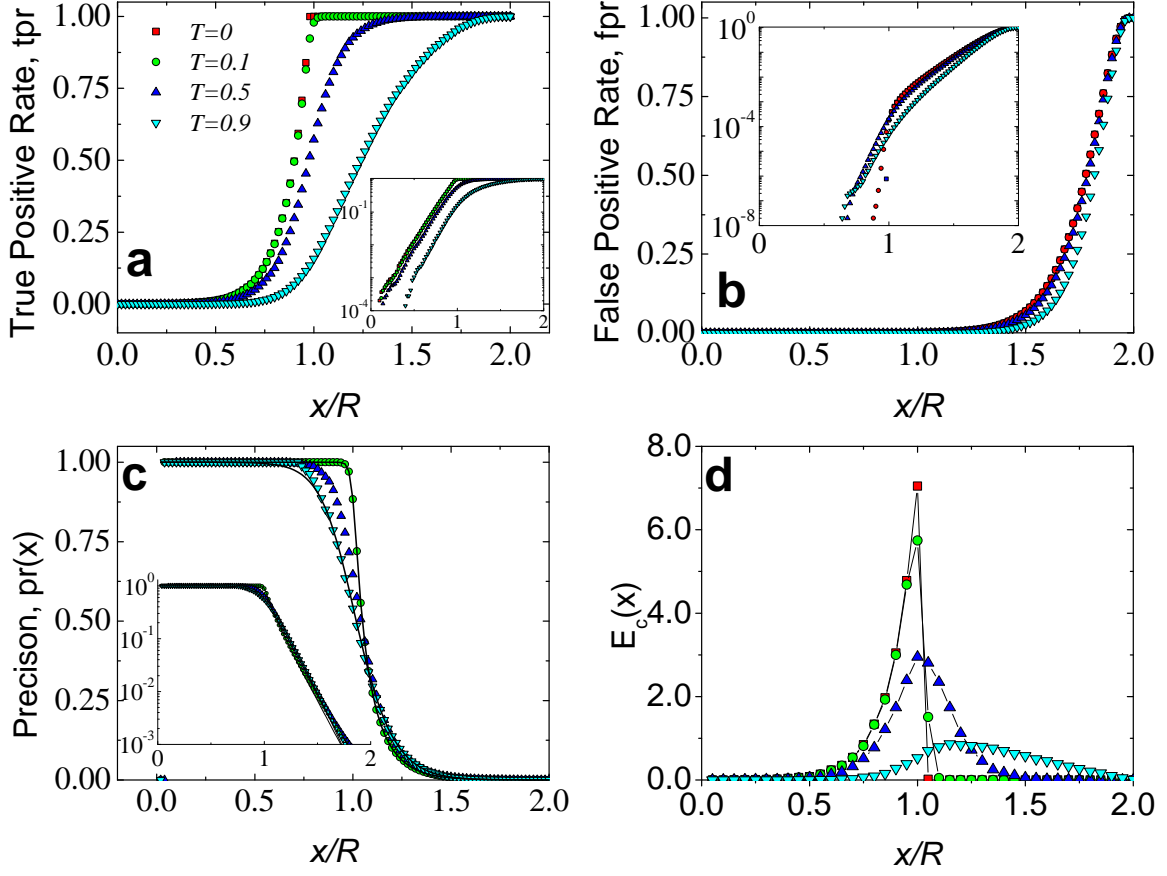


FIG. 4: **Link prediction with known coordinates.** **a**, true positive rate $\text{tpr}(x)$, **b**, false positive rate $\text{fpr}(x)$, **c**, Precision $\text{pr}(x)$ and, **d**, link density $n(x)p(x)$ as a function of hyperbolic distance x . In all experiments we remove links uniformly at random with probability $1 - q = 0.5$. Then missing links are predicted using hyperbolic distances between unconnected node pairs. All results correspond to HRG graphs with $N = 10^4$ nodes, $\gamma = 2.5$ and $\bar{k} = 10$. The insets display the same plots as the main panels but in log-linear format. Solid lines correspond to analytical estimates.

Here $E(x)$ is the cumulative number of links between the node pairs with distances up to x .

In the $T > 0$ case we rely on Eqs. (21), (24), and (39) to obtain

$$\text{tp}(x) \sim \frac{4\alpha^2(1-q)}{\pi(2\alpha-1)^2} \binom{N}{2} e^{-\frac{x-R}{2}} I\left(e^{\frac{x-R}{2}}; T\right), \quad (42)$$

$$\text{pr}(x) \sim \frac{(1-q)I\left(e^{\frac{x-R}{2}}; T\right)}{e^{\frac{x-R}{2}} - qI\left(e^{\frac{x-R}{2}}; T\right)}, \quad (43)$$

where $I(z; T)$ is given by Eq. (27).

In the $x \ll R$ regime $I\left(e^{\frac{x-R}{2}}; T\right) \sim e^{\frac{x-R}{2}}$ and $\text{pr}(x) \rightarrow 1$. In the $x \gg R$ case $I\left(e^{\frac{x-R}{2}}; T\right) \sim \frac{\pi}{T \sin(\pi/T)}$, and as a result, precision decays exponentially, $\text{pr}(x) \sim e^{-x/2}$, independent of T , Fig. 4c.

The dependence of AUPR on T arises from the recall function or its derivative, $rc'(x)$, quantifying the expected distance-dependent link density and, conse-

quently, the density of missing links.

$$rc'(x) = \frac{1}{E} \binom{N}{2} n(x)p(x). \quad (44)$$

$E_c(x)$ grows exponentially as $e^{x/2}$ for $x \ll R$ values and decays as $e^{x(1-\frac{1}{T})}$ for $x \gg R$, reaching the maximum at $x^* = R - 2T \ln\left(\frac{1}{T} - 1\right)$, Fig. 4d. Thus, as T increases, the missing links are more likely to be located at larger distances where precision $\text{pr}(x)$ is smaller, resulting in lower AUPR scores, consistent with our observations in Fig. 3.

We also note that AUPR scores have only weak dependence on node density parameter α , and consequently on degree distribution exponent $\gamma = 2\alpha + 1$. Indeed, as seen from Eqs.(41) and (40), precision and recall rates only depend on α through the node pair distribution $n(x)$, which depends on α only in sub-leading terms, as shown in Ref. [44].

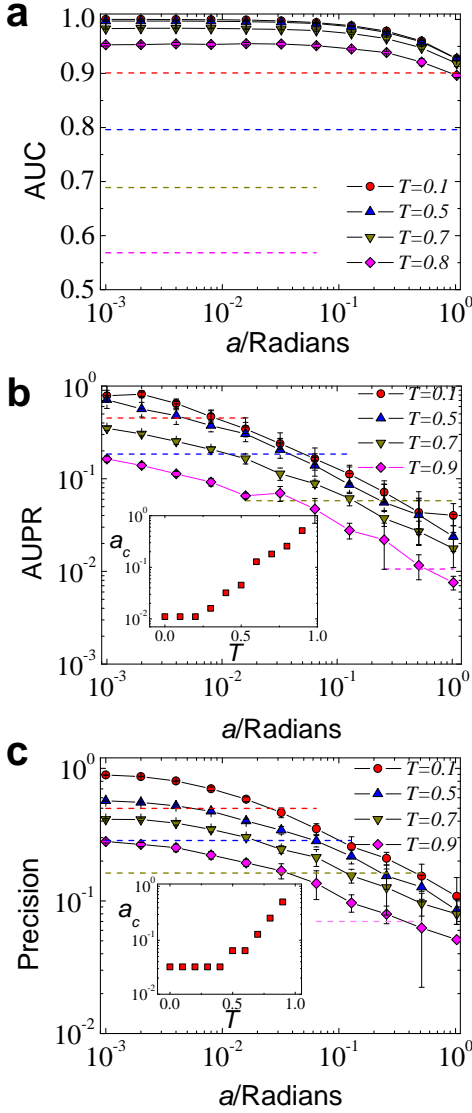


FIG. 5: **Effects of synthetic noise on link prediction accuracy.** HyperLink accuracy quantified using, **a**, AUC, **b**, AUPR, and **c**, Precision scores as a function of noise amplitude a for HRG graphs with different T values. All results correspond to HRG graphs with $N = 10^4$ nodes, $\gamma = 2.5$ and $\bar{k} = 10$. The HyperLink accuracy is compared to that of RA, i.e., its top competitor according to Fig. 3. Corresponding scores of the RA index are shown with dashed lines of matching color. The insets of panels **b** and **c** display the maximum tolerable coordinate noise amplitude as a function of T , i.e., the values of a corresponding to equal HyperLink and RA accuracy.

C. Coordinate uncertainty and link prediction accuracy

While the HyperLink provides the upper bound for link prediction on HRGs, it is important to note that its accuracy is comparable to that of other link prediction methods, in particular, Resource Allocation (RA) and Adamic Adar (AA) indexes, Fig. 3. This observation motivates the question: *How accurately does one need to infer node coordinates to ensure the superior performance*

of the HyperLink?

To answer this question we analyze the impact of node coordinate uncertainty on the HyperLink accuracy. To this end, we add synthetic noise to original angular node coordinates, while keeping radial node coordinates unchanged:

$$\hat{\theta}_i = \theta_i + aX_i, \quad (45)$$

$$X_i \sim U\left(-\frac{1}{2}, \frac{1}{2}\right), \quad (46)$$

where $a > 0$ is the noise amplitude. The effects of synthetic noise on the HyperLink accuracy are depicted in Fig. 5. Our results indicate that AUPR and Precision scores, Fig. 5b,c, decrease rapidly as a function of noise amplitude, while AUC scores remain largely unchanged even at $a > 1$ radians values.

To better understand the effects of noise on link prediction accuracy we juxtapose HyperLink prediction results to those of the RA method, which is its leading competitor according to Fig. 3. We show RA accuracy with dashed lines of matching color in Fig. 5. Consistent with our earlier observations we find that HyperLink AUC scores are robust to noise, preserving its leading ranking among other link prediction methods, Fig. 5a.

In contrast, as quantified by AUPR and Precision scores, the HyperLink is superior to the RA method only if coordinate uncertainty is sufficiently small. The maximum tolerable noise amplitude value a_c increases as T increases, see the inset of Fig. 5b,c. While noise amplitude a does not exceed 10^{-2} radians in the case of $T = 0.1$, the noise tolerance in the case of $T = 0.9$ is significantly higher, $a_c \approx 0.5$ radians, suggesting, somewhat surprisingly, that the HyperLink is better off on networks characterized by larger T values, or, equivalently, smaller clustering coefficient.

Qualitatively, the observed fast degradation of the AUPR and Precision scores is due to the sensitivity of the hyperbolic distance to the angular distance between the nodes $\Delta\theta$. It follows from Eq. (3) that even a small change in $\Delta\theta$ may significantly change the corresponding hyperbolic distance, adversely affecting the ranking of missing link candidates at small distances x , Appendix D. Since AUPR and Precision emphasize link prediction accuracy of most likely candidates, proper ranking of unconnected node pairs at small x values is crucial. AUC scores, on the other hand, place more emphasis on less obvious link candidates and are less affected by coordinate uncertainty. We find that the uniform synthetic noise adversely affects distance dependent true positive rate $\text{tp}(x|a)$, which scales as

$$\text{tp}(x|a) \sim \begin{cases} a^{1-2\gamma} & \text{if } x \leq R, \\ a^{1-2\gamma} \left(R + 2 \ln \frac{a}{2}\right) & \text{if } x > R, \end{cases} \quad (47)$$

see Appendix D, leading to

$$\text{AUPR}(a) \sim a^{2-4\gamma} \left(R + 2 \ln \frac{a}{2}\right)^2. \quad (48)$$

The robustness of the AUC scores to synthetic noise in HRGs can be qualitatively explained by the fact that AUC scores emphasize the prediction of missing links at large x distances. Large hyperbolic distances are affected by synthetic noise to the lesser extent than small hyperbolic distances. This effect follows directly from Eq. (3) and can be observed in Fig. 12a, displaying the saturation of $\text{tp}(x|a) \rightarrow 1$ as x approaches $2R$, regardless of noise amplitude a .

Our conclusions in this section are different for AUC and AUPR/Precision metrics.

The AUPR and Precision metrics emphasize prediction of the most likely missing link candidates and are highly sensitive to the accuracy of node coordinate inference. Synthetic noise added to original node coordinates smears hyperbolic distances among missing link candidates, adversely affecting the HyperLink accuracy. Our results suggest that one needs to maximize the accuracy of the network mapping in order to efficiently predict missing links. We also find that as temperature T increases, the performance of other link prediction methods, as measured by AUPR and Precision, decreases faster than that of the HyperLink, suggesting that the latter has a competitive advantage on networks characterized by large T values.

AUC scores, on the other hand, emphasize less obvious link candidates that correspond to node pairs at larger hyperbolic distances. Since larger hyperbolic distances are affected by coordinate uncertainty to the lesser extent, the AUC scores of the HyperLink are robust to synthetic noise, suggesting that HyperLink is capable of predicting less obvious missing links even under less accurate mapping conditions.

IV. LINK PREDICTION WITH INFERRED COORDINATES

In this section we build upon our results obtained in the previous section to analyze the HyperLink accuracy on networks with unknown node coordinates. We first conduct systematic analysis of HyperLink accuracy on HRGs with unknown node coordinates and then apply HyperLink to several real networks. In both cases network coordinates are unknown and in order to predict missing links we first infer node coordinates by mapping networks of interest to the 2-dimensional hyperbolic disk. To this end, we developed a mapping algorithm, which is tailored to the link prediction problem. This algorithm is referred to as the *HyperLink Embedder* and is fully described in Appendix E.

A. Tests on HRG graphs with inferred coordinates

To evaluate the HyperLink accuracy on HRG networks with unknown node coordinates we perform the following experiments. After generating an HRG network we re-

move a fraction of existing missing links. As before, each existing link is removed with probability $1 - q$. Occasionally, after links are removed, the remaining network splits into several components. If this is the case, we limit our consideration to the largest connected component of the pruned network. We refer to the resulting connected component of the pruned network as the training network. To predict missing links we erase our knowledge of the true node coordinates and then infer node coordinates by mapping the training network to the hyperbolic disk using the HyperLink Embedder, see Appendix E for details on the mapping procedure. After the mapping is complete, we use the inferred node coordinates to calculate distances between all unconnected node pairs in the training network and rank these pairs in the increasing order of distance.

Figures 6, 7, and 8 show the results for the AUPR, Precision, and AUC scores, respectively. Each panel in these figures is a heatmap, aggregating the link prediction accuracy scores for HRGs with different $\gamma \in [2.1, 2.9]$ and $T \in [0.1, 0.9]$ values, which we change with an increment of 0.1 each. We compare the HyperLink to the RA method, which is its leading competitor in these experiments, cf. Fig. 3a,b.

The results for the AUPR and Precision scores are similar. Quantified by these scores, the HyperLink accuracy is nearly independent of degree distribution exponent γ , and at the same time decreases rapidly as temperature T increases, see Figs. (6,7)a,d,g. This observation is consistent with our theoretical analysis in Section III, where we establish that AUPR scores decrease as T increases and do not strongly depend on γ .

Even though RA performs similar to HyperLink, Figs. (6,7)b,e,h, we note that RA is more accurate at lower T values and less accurate than HyperLink for higher T values. To obtain the direct comparison of the two methods we plot the difference between their AUPR (Precision) scores in Figs. 6c,f,i(7c,f,i). In agreement with our theoretical considerations in Fig. 5, we find that the HyperLink is superior to RA in the region of γ - T phase space corresponding to higher T values, these regions are demarked with dashed lines in Figs. (6,7)c,f,i.

Compared to RA, the HyperLink yields better link prediction accuracy for larger fractions of missing links. In the case $1 - q = 0.1$, for instance, HyperLink is better than RA in a small upper right corner region of the γ - T phase space, Fig. (6,7)c. On the other hand, in the case 50% of links are missing, $1 - q = 0.5$, the HyperLink outperforms RA for the majority of γ - T values with the exception of smallest, $T = 0.1$, and largest, $T = 0.9$, temperature values, Fig. (6,7)i.

The better, compared to RA, performance of the HyperLink in Fig. (6,7)i is the result of two effects. One one hand, the HyperLink accuracy appears to increase as $1 - q$ increases. This effect is consistent with a recent observation in Ref. [23] that the upper bound of link predictability in edge-independent graphs increases with $1 - q$. On the other hand, as $1 - q$ increases, the accuracy of RA de-

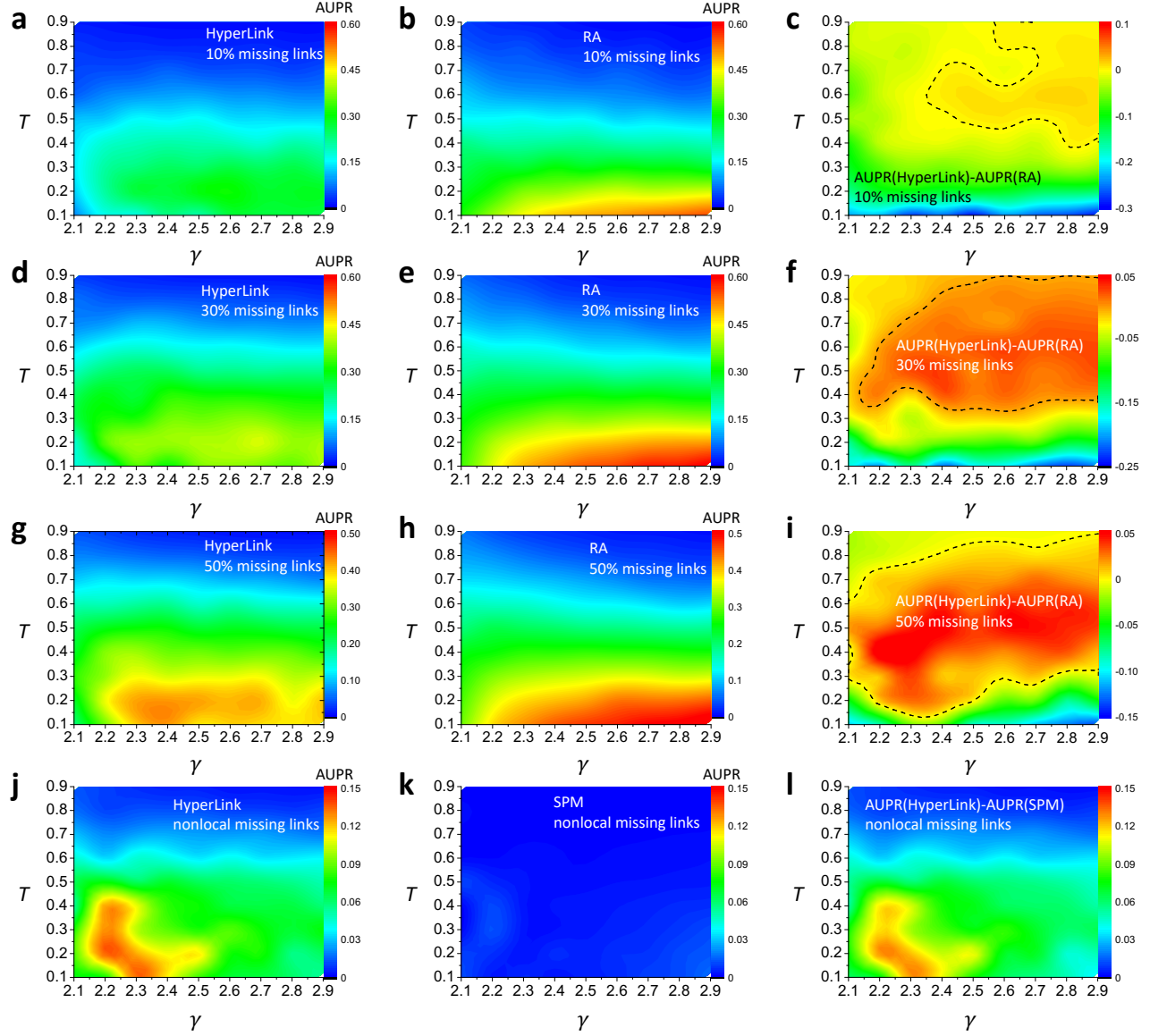


FIG. 6: **Link prediction accuracy for HRGs with inferred coordinates: AUPR.** Panels **a-i** correspond to random missing links, and **j-l** to nonlocal missing links. Each panel is a heatmap displaying AUPR values as functions of T and $\gamma = 2\alpha + 1$ parameters of the HRG model. We compare link prediction accuracy of the HyperLink to that of the RA and SPM methods, which are its leading competitors in cases of randomly missing links and nonlocal missing links, respectively. In each random missing link experiment links are removed uniformly at random with prescribed probabilities: **a-c**, $1 - q = 0.1$, **d-f**, $1 - q = 0.3$ and **g-i**, $1 - q = 0.5$. Panels **a**, **d**, **g** and **b**, **e**, **h** show the AUPR values for HyperLink and RA respectively. Panels **j-l** show the AUPR values of HyperLink and SPM, as well as their difference, for nonlocal links. i.e., links connecting nodes with no common neighbors, which are a subset of randomly removed links with $1 - q = 0.5$. The dashed curves in panels **c**, **f**, **i**, **l** demark the regions in the γ - T parameter space where the HyperLink accuracy is higher than that of the competitive method.

creases. RA, as well as other similarity-based methods, e.g., RA, CRA, AA, CN and JC, predict missing links based on the similarity of node neighborhoods, e.g, the number of common neighbors, the higher the similarity the higher the probability of a missing link, Appendix B. Neighborhood similarities are local measures, reflecting network structure in the network-based vicinity of the node pair of interest, and ignoring the structure of the remaining network. The larger the fraction of missing

links, the smaller is the fraction of links in the training network, and as a result, the poorer the link prediction results. While this is true for all link prediction methods, the similarity-based methods are the ones that suffer most. Since links are established independently in HRGs, and each link is removed with probability $p = 1 - q$, the number of common neighbors between any node pairs on average decreases proportionally to p^2 . All extensive HRG properties, on the other hand, depend on p linearly.

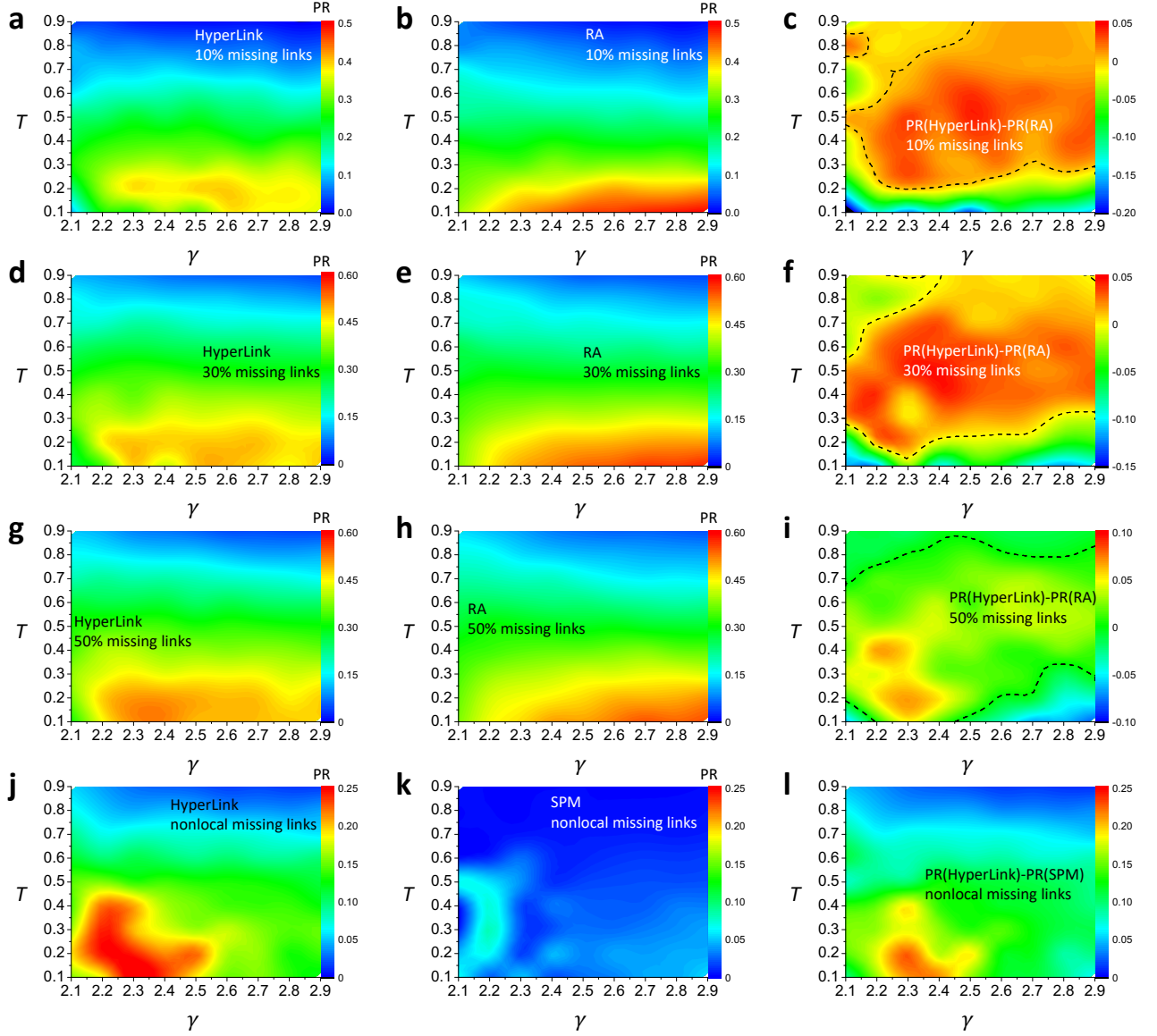


FIG. 7: Link prediction accuracy for HRGs with inferred coordinates: Precision. The legend is identical to that of Fig. 6.

HyperLink as a global method uses the structure of the entire network to map it, so that it is less sensitive to network incompleteness.

An attractive feature of a global method is that it is capable of predicting *nonlocal missing links*, i.e., links between node pairs with no common neighbors. To quantify HyperLink accuracy for nonlocal links we consider the subset of nonlocal links within the set of links removed with probability $1 - q = 0.5$, Fig. (6,7)j, which comprise from 20% (for $\gamma = 2.1$, $T = 0.9$) to 86% (for $\gamma = 2.9$, $T = 0.1$) of all removed links.

Similarity-based methods, RA, AA, CN, and JC, cannot predict nonlocal missing links since corresponding node pairs have no common neighbors at all, and, consequently, have zero similarity. Therefore, in nonlocal

link prediction experiments we compare HyperLink to SPM index, which is a global method and the leading competitor to HyperLink for nonlocal links. As seen in Figs. (6,7)k,l, SPM index yields substantially lower link prediction accuracy than HyperLink for all the considered values of γ and T .

Overall, we observe that according to the AUPR and Precision scores, HyperLink's competitive advantage is the higher, the more incomplete the network is, and the HyperLink is particularly strong in prediction nonlocal links.

According to AUC scores, the HyperLink offers superior link prediction accuracy across the entire γ - T parameter space, surpassing its leading competitors—RA for all links, and SPM for nonlocal links, Fig. 8. This

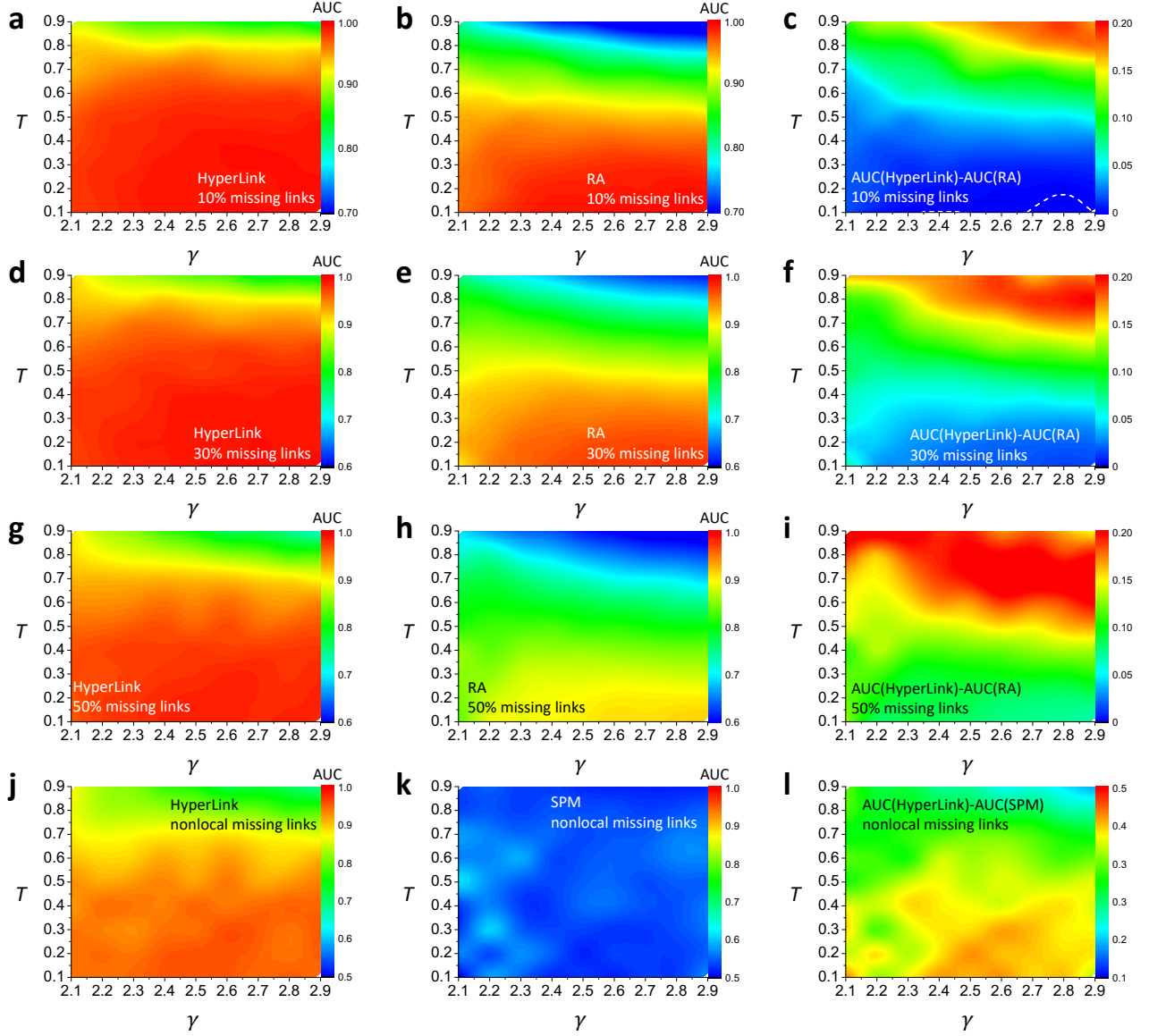


FIG. 8: Link prediction accuracy for HRGs with inferred coordinates: AUC. The legend is identical to that of Fig. 6.

result is again consistent with our calculations in Section III showing that HRG-based AUC scores are robust with respect to coordinate uncertainty.

B. Tests on real networks

Finally, we apply the HyperLink to real networks: the Internet at the Autonomous System level [45], the network of human metabolism [46], and the Pretty-Good-Privacy (PGP) web of trust [47]. Basic properties of these networks as well as the data curation steps are discussed in Appendix A.

Our link prediction experiments on real networks are performed identically to those on HRG networks with

inferred coordinates, and the results are shown in Figs. 9, 10, and 11.

According to AUPR and Precision metrics, the HyperLink offers competitive performance in random link removal experiments, Figs. 9-11a - f, but, at the same time, is not the most accurate, except for the case of the Internet at $1 - q = 0.5$, Fig. 9d. We do note that the relative performance of the HyperLink is better in cases of higher missing link rate, $1 - q = 0.5$, which is consistent with our results in HRG networks.

We also note that the HyperLink offers superior performance in prediction of nonlocal links where it is the best, with SPM method being its leading competitor, Figs. 9g-i, 10g-i, and 11g-i. This observation comes in sharp contrast with nearly random performance of similarity based

methods, RA, AA, CN, JC, and CRA, in nonlocal link prediction.

By examining Precision-Recall curves in Figs. 9, 10, and 11 we observe that Precision scores of the HyperLink exceed those of its competitors for larger Recall values. This observation supports our earlier conclusions that HyperLink performs best at identifying *hard-to-predict* links.

In contrast to AUPR-based rankings where HyperLink is rarely the most accurate method, HyperLink is ranked best in all experiments according to the AUC metric, in agreement with all the AUC-related results above.

V. DISCUSSION

Parameter	AUC	AUPR, Precision
Exponent $\gamma \in (2, 3)$	$\approx \text{const}$	$\approx \text{const}$
Temperature $T \in (0, 1)$	$\approx \text{const}$	decreasing
Fraction of missing links $1 - q$	increasing	increasing
Noise amplitude a	$\approx \text{const}$	decreasing

TABLE I: The summary of the results in Section III: HyperLink’s measures of accuracy of link prediction in HRGs with known node coordinates as functions of the parameters in Section III.

Scenario	AUC	AUPR, Precision
HRGs with inferred coordinates	Best	Best if T , γ , or $1 - q$ is large
Real networks	Best	The more competitive, the larger the $1 - q$
Nonlocal links in HRGs and real networks	Best	Best

TABLE II: The summary of the results in Section IV: HyperLink’s measures of accuracy of link prediction in HRGs with inferred coordinates and in real networks, as well as those for nonlocal links, compared to other methods. The parameters are the same as in Table I.

Tables I and II summarize the results in Sections III and IV, respectively. We see that when it comes to predicting obvious missing links that are easy to predict, then employing hyperbolic geometry may be not the best way to proceed. One can safely use a variety of other methods that may be better at this task, according to the AUPR or Precision measures. This is because most obvious missing links are the links between closest nodes in the latent hyperbolic space, and to rank them exactly at the top of the disconnected node pair list, one has to infer the coordinates nearly exactly, Section III.

However, if the task is to identify missing links that are really hard to predicts, then this is where hyperbolic network geometry should be used. The most striking example is the prediction of missing links between nodes that do no share any common neighbors. Here the HyperLink is by far the best, according to all the AUC,

AUPR, and Precision measures, in all the considered real and synthetic networks. It is not surprising that local methods do a poor job in predicting such links—they are simply not designed to do so. In contrast, the HyperLink is not a local but global method, taking the whole network structure into account, but so is the highly advanced SPM method that outperforms a vast collection of other methods according to [48], and we see that the HyperLink outperforms even it by far at this task.

We also see that according to the AUC measure, the HyperLink is also the best in all the considered situations. This is because the AUC does not care that much about false positives, in which case the HyperLink achieves the best balance between the true and false positive rates by doing better than any other method in finding missing links between highly dissimilar nodes located at large distances in the latent hyperbolic space.

We have also shown that the HyperLink is the better off, the weaker the clustering (the higher the T), and the larger the fraction of missing links $1 - q$ in HRGs with inferred coordinates. This does not mean that HyperLink’s link prediction accuracy scores are getting better in these more difficult conditions; its scores do degrade. But the speed of the degradation of these that the other methods experience are higher than HyperLink’s.

Overall, it appears to be that the harder a specific link prediction task is, the better the HyperLink is at this task.

Our results also resolve the controversy among earlier reports on link prediction using hyperbolic geometry [23, 32–36]. These reports approached link prediction using different measures of link prediction accuracy. To reiterate, if applied to sparse networks, the AUPR emphasizes the prediction of a small fraction of the most likely missing links and, as a result, is extremely sensitive to inaccuracies in the node coordinate inference. On the other hand, the AUC is more robust to coordinate uncertainties as it emphasizes the prediction of less likely missing links between dissimilar nodes at large latent distances.

To maximize HyperLink’s link prediction accuracy, we have developed a new hyperbolic network mapping method, the HyperLink Embedder, that maximizes the accuracy of coordinate inference. Its accuracy comes at the computational complexity cost of $O(n^2)$. While faster methods for hyperbolic mapping have been developed recently [49–53], an optimal balance between the accuracy and speed of hyperbolic mapping is still to be found. Ideally, it would be highly desirable to have a method that would be as accurate as at least the HyperLink Embedder, and that would run in $O(n)$ time.

Finally, we emphasize that link prediction using latent hyperbolic geometry is expected to yield best results only if this geometry is there in a given network. That is, the network structure must be consistent with the existence of this geometry. It is well known that HRGs are characterized by sparsity, self-similarity, scale-free degree distributions, and strong clustering, meaning that these prop-

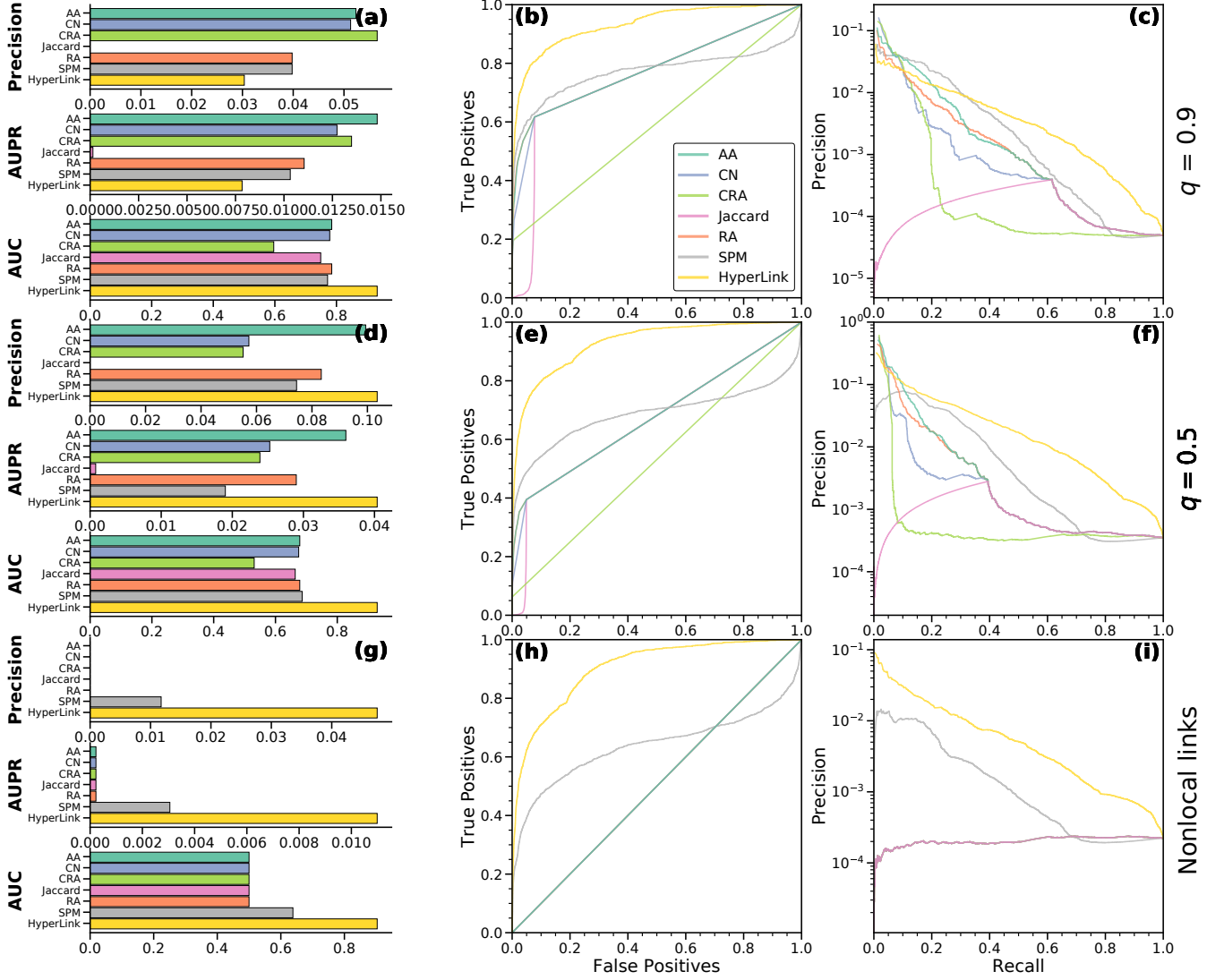


FIG. 9: Link prediction accuracy for the Internet with **a-c** 10% ($q=0.9$) randomly missing links, **d-f** 50% ($q=0.5$) randomly missing links, and **g-i** nonlocal missing links, i.e., links connecting node pairs that have no common neighbors. Nonlocal links constitute 32% of the $q = 0.5$ missing links set. Panels **a, d, g, j** depict Precision, AUPR, and AUC link prediction scores. Panels **b, e, h, k** and **c, f, i, l** show, respectively, the ROC and PR curves.

erties are necessary conditions for hyperbolic geometry presence. It is also well known that many real networks do possess these properties as well. The results in [31] suggest that clustering is also a sufficient condition for network geometricity, but these results apply only to homogeneous large-world networks, and ignore coordinate entropy. In other words, the detailed sufficient conditions for the presence of latent hyperbolic geometry are currently unknown, remaining a subject of ongoing research.

VI. ACKNOWLEDGEMENTS

We thank R. Aldecoa, F. Papadopoulos, C. V. Canistraci and M. Á. Serrano for useful discussions and suggestions. This work was supported ARO Grant No. W911NF-17-1-0491 and NSF Grant No. IIS-1741355.

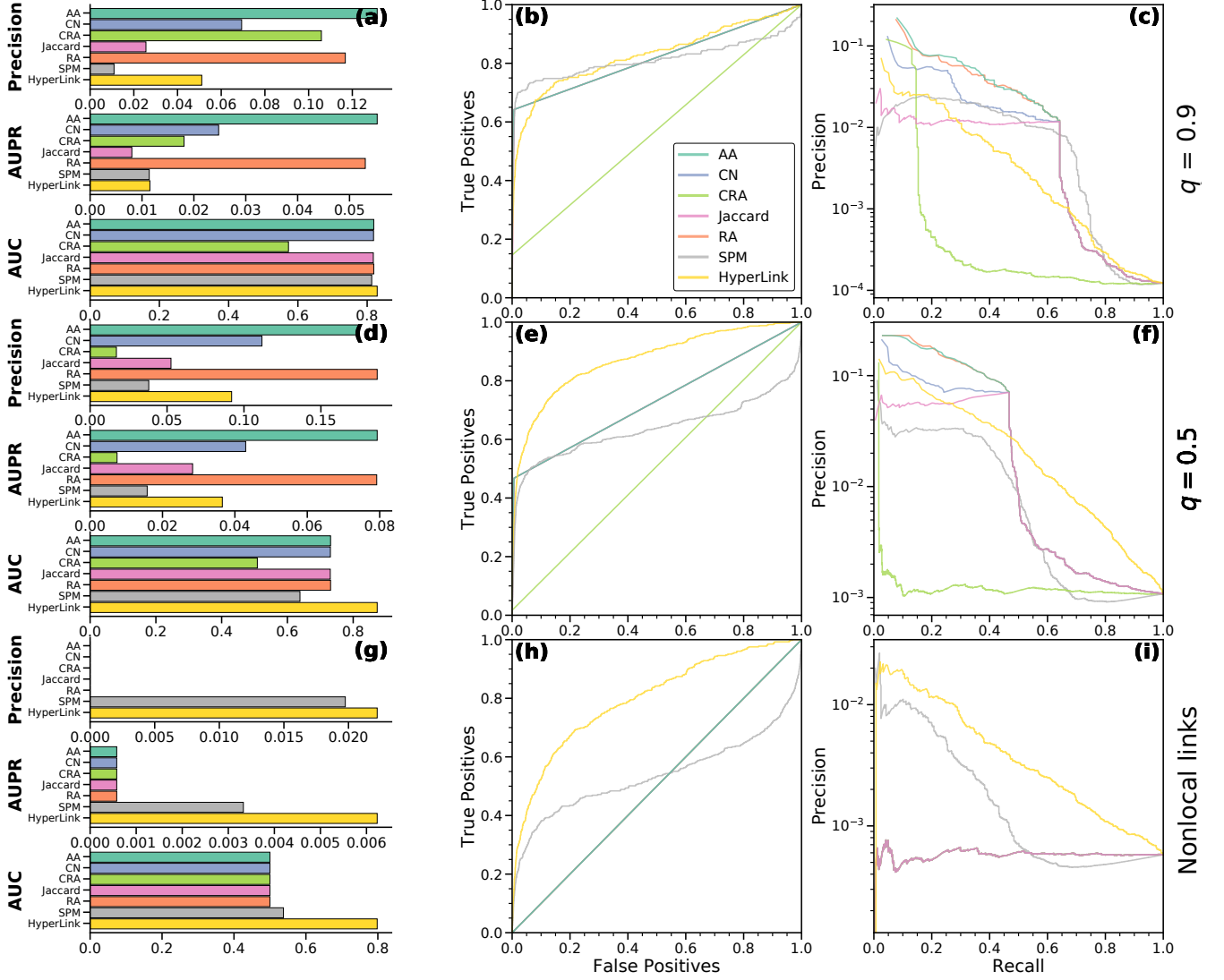


FIG. 10: Link prediction accuracy for the Metabolic network. Panels are identical to those of Fig. 9. Nonlocal links constitute 20% of the $q = 0.5$ missing links set.

Appendix A: Real Networks

1. Internet

The Internet network is a snapshot of the Autonomous System level Internet taken from the University of Oregon Route Views Project [45]. The full dataset contains 733 daily instances which span an interval of 785 days from November 8 1997 to January 2 2000. Here we use a network instance as of January 2, 2000. Further details on the dataset can be found at <http://snap.stanford.edu/data/as.html>.

2. Metabolic network

The Metabolic Network is based on the dataset of metabolic interactions of 107 organisms constructed by H. Ma and A.-P. Zheng [46]. Original network is bipartite and consists of metabolites (top domain) connected to chemical reactions (bottom domain). We consider the unipartite projection of the network on the top domain. Basic properties of the Metabolic network are summarized in Table III.

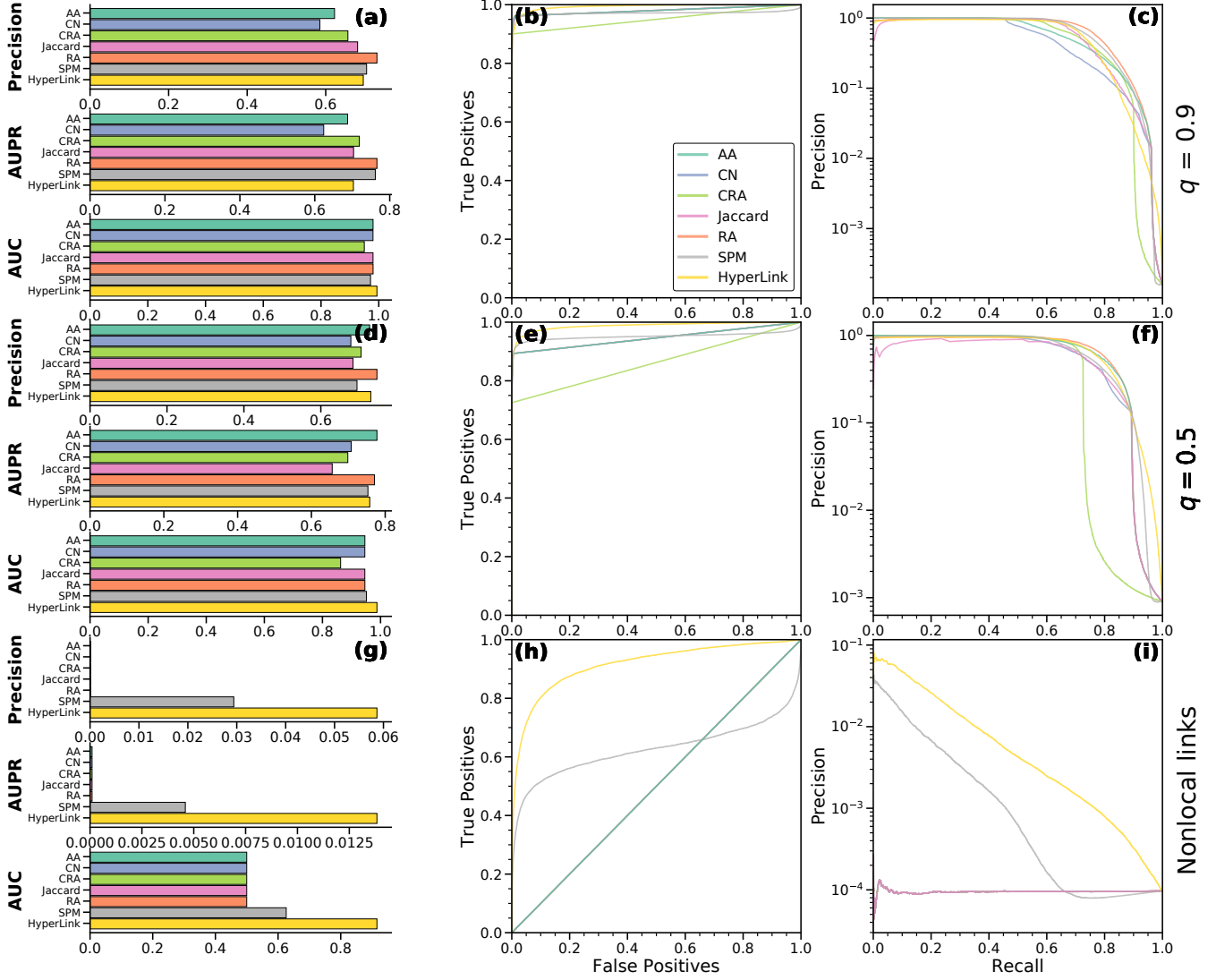


FIG. 11: Link prediction accuracy for the PGP network. Panels are identical to those of Fig. 9. Nonlocal links constitute 10% of the $q = 0.5$ missing links set.

3. PGP web of trust

Pretty-Good-Privacy (PGP) is a data encryption and decryption computer program that provides cryptographic privacy and authentication for data communication [47]. The data is collected and maintained by Jörgen Cederlöf [54]. In the manuscript we use the PGP snapshot taken in April of 2003. PGP web of trust is a directed network where nodes are certificates consisting of public PGP keys and owner information. A directed link in the web of trust pointing from certificate A to certificate B represents a digital signature by owner of A endorsing the owner/public key association of B. We construct the undirected PGP graph by taking into account only bi-directional trust links between the certificates. Further, we only consider the Giant Connected Component of the resulting undirected PGP web of trust network. Basic properties of the PGP network are summarized in Table III.

Network name	N	E	\bar{k}	γ	\bar{c}	\bar{T}
Internet	6,474	13,234	4.09	2.1	0.51	0.7
Metabolic network	2,732	4,040	2.96	2.9	0.29	0.6
PGP web of trust	14,138	160,080	22.65	2.1	0.66	0.8

TABLE III: Basic properties of the considered real networks. N is the number of top nodes, E is the number of edges, \bar{k} is the average degree, γ is the degree distribution exponent, which we estimated using methods from Ref. [55], \bar{c} is the average degree-dependent clustering coefficient, and T is the corresponding HRG temperature.

Appendix B: Link Prediction: Alternative Methods and Scoring Techniques

1. Alternative Methods

We compare the accuracy of the HyperLink link prediction method against the following set of link-prediction methods: Common Neighbors (CN) [56], Adamic and Adar (AA) [7], Resource Allocation (RA) [57], Local Community Resource Allocation (CRA) [58], Jaccard's index (JC) [59], and Structural Perturbation Method (SPM) [48]. All these methods, as well as HyperLink, assign scores to (a subset of) all not directly connected pairs of nodes (non-links), and all such pairs are then ranked according to these scores from the most to least likely interaction prediction. To briefly describe these methods, it is thus sufficient to tell how these scores are calculated, for which we use the following notations: k_i the degree of node i ; $\Gamma(i)$ the set of i 's neighbors (directly connected nodes); $\gamma_{ij}(s)$ the subset of $\Gamma(s)$ that are neighbors of both i and j ; e_i^j , i 's j -external degree, the number of i 's neighbors that are *not* j 's neighbors; \mathbf{A} is the network adjacency matrix. *Common Neighbors (CN)*. The score for a pair of nodes i and j is defined as the cardinality of the intersection of their sets of neighbors,

$$s_{ij}^{CN} = |\Gamma(i) \cap \Gamma(j)|. \quad (\text{B1})$$

Jaccard's index (JC). The score is a normalized measure of the overlap of i 's and j 's sets of neighbors,

$$s_{ij}^{JC} = \frac{|\Gamma(i) \cap \Gamma(j)|}{|\Gamma(i) \cup \Gamma(j)|}. \quad (\text{B2})$$

Adamic-Adar index (AA). The score assigns more weight to the less-connected neighbors,

$$s_{ij}^{AA} = \sum_{s \in \Gamma(i) \cap \Gamma(j)} \frac{1}{\log k_s}. \quad (\text{B3})$$

Resource Allocation index (RA). The score is similar to the AA score, but punishes high-degree nodes more strongly,

$$s_{ij}^{RA} = \sum_{s \in \Gamma(i) \cap \Gamma(j)} \frac{1}{k_s}. \quad (\text{B4})$$

Local Community Resource Allocation index (CRA). The score is similar to the RA score, but takes into account the subset of nodes shared between nodes i , j and their common neighbors s :

$$s_{ij}^{CRA} = \sum_{s \in \Gamma(i) \cap \Gamma(j)} \frac{\gamma_{ij}(s)}{k_s}. \quad (\text{B5})$$

Structural Perturbation Method (SPM). This method is based on repetitive perturbations of the adjacency matrix \mathbf{A} by removals of small fractions of links that we denote by ΔE . The original adjacency matrix can then be written as $\mathbf{A} = \mathbf{A}' + \Delta \mathbf{A}$, where \mathbf{A}' is the adjacency matrix of the network after removal of links ΔE , and $\Delta \mathbf{A}$ is the adjacency matrix constructed on the set of removed links ΔE . Denoting eigenvectors and eigenvalues of \mathbf{A}' by x_k and λ_k , the perturbations of the original eigenvalues λ_k using the perturbation matrix $\Delta \mathbf{A}$, are

$$\Delta \lambda_k \approx \frac{x_k^T \Delta \mathbf{A} x_k}{x_k^T x_k}, \quad (\text{B6})$$

so that the perturbed adjacency matrix is

$$\tilde{\mathbf{A}} = \sum_{k=1}^N (\lambda_k + \Delta \lambda_k) x_k x_k^T. \quad (\text{B7})$$

All non-links i, j are then ranked by \tilde{A}_{ij} . In our experiments we repeat this perturbation procedure 10 times, and then average perturbed matrices over these trials, thus obtaining an averaged perturbed matrix $\langle \tilde{\mathbf{A}} \rangle$, so that the SPM score is

$$s_{ij}^{SPM} = \langle \tilde{A}_{ij} \rangle. \quad (\text{B8})$$

Appendix C: Basic properties of the HRG model

The hyperbolic geometry inference algorithm relies on several properties of the HRG model, which we review in this section.

Degree distribution. HRG models are characterized by scale-free degree distributions, $P(k) \sim k^{-\gamma}$, where $\gamma = 2\alpha + 1$. Indeed, the expected degree of a node located at (r, θ) is independent of its angular coordinate θ , $\bar{k}(r, \theta) = \bar{k}(r, 0) = \bar{k}(r)$, and is given by

$$\begin{aligned} \bar{k}(r) &= (N-1) \int dr' \rho(r') \int d\theta' \rho(\theta') p[x(r, 0, r', \theta')] \\ &\approx \frac{4N\alpha}{2\alpha-1} \frac{T}{\sin \pi T} e^{-r/2}, \end{aligned} \quad (\text{C1})$$

see [19]. The average degree of the model is given by

$$\bar{k} = \int dr \rho(r) \bar{k}(r) = \frac{8N\alpha^2}{(2\alpha-1)^2} \frac{T}{\sin \pi T} e^{-R/2}. \quad (\text{C2})$$

As seen from Eq. (C2), \bar{k} in the most general case depends on the network size N .

To achieve sparse models with \bar{k} independent of N one sets the radius of the hyperbolic disk to

$$R(N) = 2 \ln(N/\nu), \quad (\text{C3})$$

where $\nu > 0$ is the tuning parameter, directly related to \bar{k} . Indeed, with $R(N)$ given by (C3)

$$\bar{k} = \frac{8\nu\alpha^2}{(2\alpha-1)^2} \frac{T}{\sin \pi T}, \quad (\text{C4})$$

prescribing the value of ν for the target values of \bar{k} , α and T .

It has been shown in [60] that in the sparse limit the probability of a node located at (r, θ) to have k connections can be approximated with the Poisson distribution with the mean of $\bar{k}(r)$:

$$P(k|r) = e^{-\bar{k}(r)} \frac{[\bar{k}(r)]^k}{k!}. \quad (\text{C5})$$

Then degree distribution of the HRG is

$$P(k) = \int dr \rho(r) P(k|r) \sim k^{-\gamma}, \quad (\text{C6})$$

$$\gamma = 2\alpha + 1. \quad (\text{C7})$$

It follows from Eqs. (C1) and (C4) that model parameters α and R can be used to control degree distribution exponent γ and the average degree of the model, respectively.

Clustering coefficient. As seen from Eq. (6), connection probability $p(x)$ decreases exponentially for distances $x > R$ with the rate of $\frac{1}{2}T$. Thus, the temperature parameter T , tunes the role of large distances in the formation of links: the higher the T the more likely are long-distance connections. As a result, T controls the clustering coefficient of the HRG. In the $T \rightarrow 0$ limit connections are only possible at hyperbolic distances $x < R$ and the clustering coefficient is maximized. Conversely, the clustering coefficient decreases as T increases and vanishes asymptotically in the $T \geq 1$ case [19].

Appendix D: Effects of Coordinate Uncertainty on HyperLink Accuracy

To understand the effects of coordinate uncertainties on HyperLink accuracy we model coordinate inference uncertainty as synthetic noise that we add to true angular coordinates of the HRG graph. In the following we first generate HRG as described in Section II B and then simulate uncertainties of angular coordinates by adding synthetic noise to original angular coordinates:

$$\hat{\theta}_i = \theta_i + a(\ell)X_i, \quad (\text{D1})$$

$$X_i \sim U\left(-\frac{\pi}{2}, \frac{\pi}{2}\right), \quad (\text{D2})$$

where $a > 0$ is the noise amplitude. Further, we conduct link prediction experiments by calculating latent distances with uncertain coordinates:

$$\hat{x}_{ij} = x(r_i, \hat{\theta}_i, r_j, \hat{\theta}_j), \quad (\text{D3})$$

where x is calculated according to the hyperbolic law of cosines, Eq. (3)

1. Link prediction with noise

In the case of synthetic noise, the AUPR scores are still given Eq. (36) with effective precision and recall rates $\text{pr}(x|a)$ and $\text{rc}(x|a)$ evaluated in presence of noise. To calculate these rates we start with the effective true positive rate $\text{tp}(x|a)$.

To this end, we first define the subgraph G_y obtained from the HRG G by keeping only links between node pairs separated by distances at most y . Then, it is easy to realize that the true positive rate $\text{tp}(y)$ is proportional to the expected degree \bar{k}_y of the G_y :

$$\text{tp}(y) = (1 - q) \frac{N}{2} \bar{k}_y. \quad (\text{D4})$$

\bar{k}_y can be calculated using the hidden variable formalism:

$$\bar{k}_y = (N - 1) \int \cdots \int_{x(r_1, \theta_1, r_2, \theta_2) \leq y} dr_1 dr_2 d\theta_1 d\theta_2 \rho(r_1) \rho(r_2) \rho(\theta_1) \rho(\theta_2) p[x(r_1, \theta_1, r_2, \theta_2)] \quad (\text{D5})$$

To account for noise we next define noisy subgraph $G_y(a)$ as follows. First, noise is added to node coordinates of the original HRG as prescribed by Eq. (45) and hyperbolic distances between nodes are recalculated using the updated coordinates. Second, $G_y(a)$ is formed from HRG by keeping connections at *recalculated* distances up to y . It is then easy to see that the thought true positive rate is given by

$$\text{tp}(y|a) = (1 - q) \frac{N}{2} \bar{k}_y(a), \quad (\text{D6})$$

where $\bar{k}_y(a)$ is the average degree of noisy subgraph $G_y(a)$.

After a series of tedious calculations, which we detail in the Subsection D 2, we obtain the leading order behavior of $\bar{k}_x(a)$

$$\bar{k}_x(a) \begin{cases} Ng(x)a^{1-2\alpha} & \text{if } x \leq R, \\ Ng(x)a^{1-2\alpha} [R + 2 \ln \frac{a}{2}] & \text{if } x \geq R, \end{cases} \quad (\text{D7})$$

where $\alpha \in (\frac{1}{2}, 1)$ is the radial node density parameter in Eq. (5) corresponding to degree distribution exponent $\gamma = 2\alpha + 1$. Similar to the noiseless case, $g(x)$ grows as $\exp(\frac{x}{2})$ for $x < R$ and saturates to a constant value, corresponding to $\bar{k}_x(a) = \bar{k}$ as $x \rightarrow 2R$, Fig. 12a.

Using Eq.(40) one can rewrite the distance-dependent precision function as

$$\text{pr}(x|a) = \frac{\text{tp}(x|a)}{\binom{N}{2} \int_0^x n(y|a) dy - \frac{q}{1-q} \text{tp}(x|a)}, \quad (\text{D8})$$

where $n(x|a)$ is the node pair distribution in the hyperbolic disk with coordinate noise.

Due to the uniform initial angular distribution $\rho(\theta)$, the node pair distribution is independent of noise, $n(x|a) = n(x)$, Fig. 12b. Further, in the case of sufficiently large noise amplitude a , $\text{tp}(x|a) \ll \binom{N}{2} \int_0^x n(y|a) dy$ and

$$\text{pr}(x|a) \approx \frac{\text{tp}(x|a)}{\binom{N}{2} \int_0^x n(y) dy}. \quad (\text{D9})$$

As a result, in the case $x < R$ $\text{pr}(x|a) \sim a^{1-2\alpha}$, see Fig. 12c.

Since distance-dependent recall function is proportional to the true positive rate,

$$\text{rc}(x|a) = \frac{\text{tp}(x|a)}{(1-q)E}. \quad (\text{D10})$$

resulting AUPR score scales as

$$\text{AUPR}(a) \sim a^{2-4\alpha} \left[A + B \left(R + 2 \ln \frac{a}{2} \right)^2 \right], \quad (\text{D11})$$

where

$$A = \frac{1-q}{E} \binom{N}{2} \int_0^R \frac{dx g(x) g'(x)}{n^c(x)}, \quad (\text{D12})$$

$$B = \frac{1-q}{E} \binom{N}{2} \int_R^{2R} \frac{dx g(x) g'(x)}{n^c(x)} \quad (\text{D13})$$

see Fig. 12d.

This result suggest that the impact of coordinate uncertainty on link prediction is higher in HRG with larger $\gamma = 2\alpha + 1$ values. Intuitively, this is the case since networks with larger γ values have larger fractions of small degree nodes. Small degree nodes in the HRG are characterized by large radial coordinates, and hyperbolic distance between point with large radial coordinates are most affected by angular coordinate uncertainties.

2. The average degree of the noisy subgraph

Here we derive the leading term behavior of the average degree of the noisy subgraph $G_y(a)$ for $y < R$.

As shown in the subsection above, the number of true positives $\text{tp}(y|a)$ is related to the average degree of noisy subgraph $G_y(a)$. To define $G_y(a)$ we add uniform noise of amplitude a to original angular coordinates of the HRG and calculate noisy hyperbolic distances \tilde{x}_{ij} between all node pairs using noisy coordinates. $G_y(a)$ is the HRG subgraph formed by node pairs with noisy hyperbolic distances $\tilde{x}_{ij} < y$. The average degree of $G_y(a)$ is given by

$$\bar{k}_y(a) = (N-1) \int \cdots \int_{x(r_1, \hat{\theta}_1, r_2, \hat{\theta}_2) \leq y} dr_1 dr_2 d\hat{\theta}_1 d\theta_1 d\hat{\theta}_2 d\theta_2 \rho(r_1) \rho(r_2) \rho(\hat{\theta}_1) \rho(\theta_1 | \hat{\theta}_1) \rho(\hat{\theta}_2) \rho(\theta_2 | \hat{\theta}_2) p[x(r_1, \theta_1, r_2, \theta_2)]. \quad (\text{D14})$$

Here $\rho(r)$ is given by Eq. (5), and $\rho(\theta | \hat{\theta})$ is the conditional probability of the true angle θ , given inferred angle $\hat{\theta}$. In case of the uniform noise, $\rho(\theta | \hat{\theta})$ is also a uniform distribution centered at $\hat{\theta}$:

$$\rho(\theta | \hat{\theta}) = U\left(\hat{\theta} - a/2, \hat{\theta} + a/2\right), \quad (\text{D15})$$

while

$$\rho(\hat{\theta}) = \rho(\theta) = \frac{1}{2\pi}. \quad (\text{D16})$$

Throughout the calculation of $k_y(a)$ we will rely on the number of assumptions. We are primarily interested in HRGs with $2 < \gamma < 3$, which correspond to $\frac{1}{2} < \alpha < 1$. Further, we focus on the values of $y > R/2$ since these values allow us to simplify calculations. One can justify this constraint since the number of node pairs in HRG is very small for $y \leq R/2$. To identify leading terms we will also recall on the scaling of R with the system size, $N \sim e^{\frac{R}{2}}$.

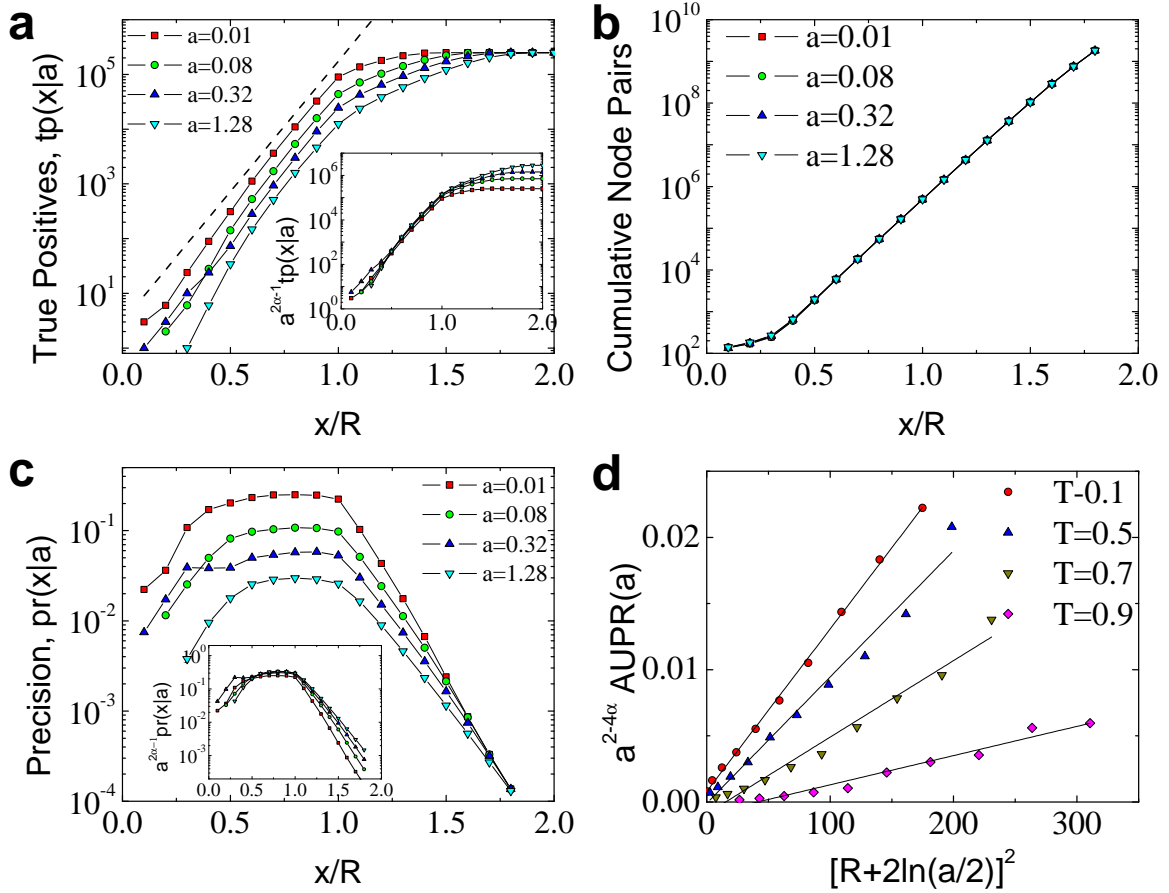


FIG. 12: **HyperLink accuracy in case of coordinate uncertainty.** All plots correspond to HRG graphs of $N = 10^5$ nodes, $\gamma = 2.5$ ($\alpha = 0.75$), $T = 0.1$ and $\bar{k} = 10$. **a**, Distance-dependent true positive rate $tp(x|a)$ evaluated for different noise amplitude values. For $x < R$, $tp(x|a)$ grows as $e^{x/2}$, see the dashed line for the reference. The inset tests the scaling of $tp(x|a) \sim a^{1-2\alpha}$ for $x < R$. **b**, The cumulative number of node pairs in the hyperbolic disc as a function of hyperbolic distance between the nodes. Note that the cumulative number of node pairs is independent of noise amplitude. **c**, Distance-dependent precision rate $pr(x|a)$ for different a values. $pr(x|a)$ is nearly constant for $x < R$ since both $tp(x|a)$ and $n(x|a)$ grow as $e^{x/2}$. $pr(x|a)$ decays as $e^{-x/2}$ for $x > R$. The inset test the scaling of $pr(x|a) \sim a^{1-2\alpha}$ for $x < R$. **d**, The scaling test for AUPR(a) of the HRG with $N = 5000$, $\gamma = 2.5$, and $\bar{k} = 10$. Note that $a^{4\alpha-2} \text{AUPR}(a)$ grows linearly as a function of $(R + 2 \ln \frac{a}{2})^2$, confirming Eq. (D11).

Since hyperbolic distance x in Eq. (3) depends on θ_1 and θ_2 only through their difference,

$$x(r_1, \theta_1, r_2, \theta_2) = x(r_1, r_2, \Delta\theta_{12}), \quad (\text{D17})$$

$$\Delta\theta_{12} \equiv \pi - |\pi - |\theta_1 - \theta_2||, \quad (\text{D18})$$

and angles distributed uniformly on $[-\pi, \pi]$, $\rho(\hat{\theta}_{1,2}) = \frac{1}{2\pi}$ we can simplify Eq. (D14) as

$$\bar{k}_y(a) = \frac{N}{(2\pi)^2} \int \cdots \int_{x(r_1, r_2, \Delta\hat{\theta}_{12}) \leq y} dr_1 dr_2 \rho(r_1) \rho(r_2) d\hat{\theta}_1 d\hat{\theta}_2 d\Delta\theta \tilde{\rho}(\Delta\theta_{12} | \Delta\hat{\theta}_{12}) p[x(r_1, r_2, \Delta\theta_{12})], \quad (\text{D19})$$

where

$$\tilde{\rho}(\Delta\theta_{12} | \Delta\hat{\theta}_{12}) = \frac{1}{a^2} \Theta(a - |\Delta\theta_{12} - \Delta\hat{\theta}_{12}|), \quad (\text{D20})$$

and $\Theta[x]$ is the Heaviside Theta function. Similar to the calculation of \bar{k} in the HRGs, Ref. [19], we can rewrite Eq. (D19) as

$$\bar{k}_y(a) = \int_0^R dr_1 \rho(r_1) \bar{k}_y(r_1 | a), \quad (\text{D21})$$

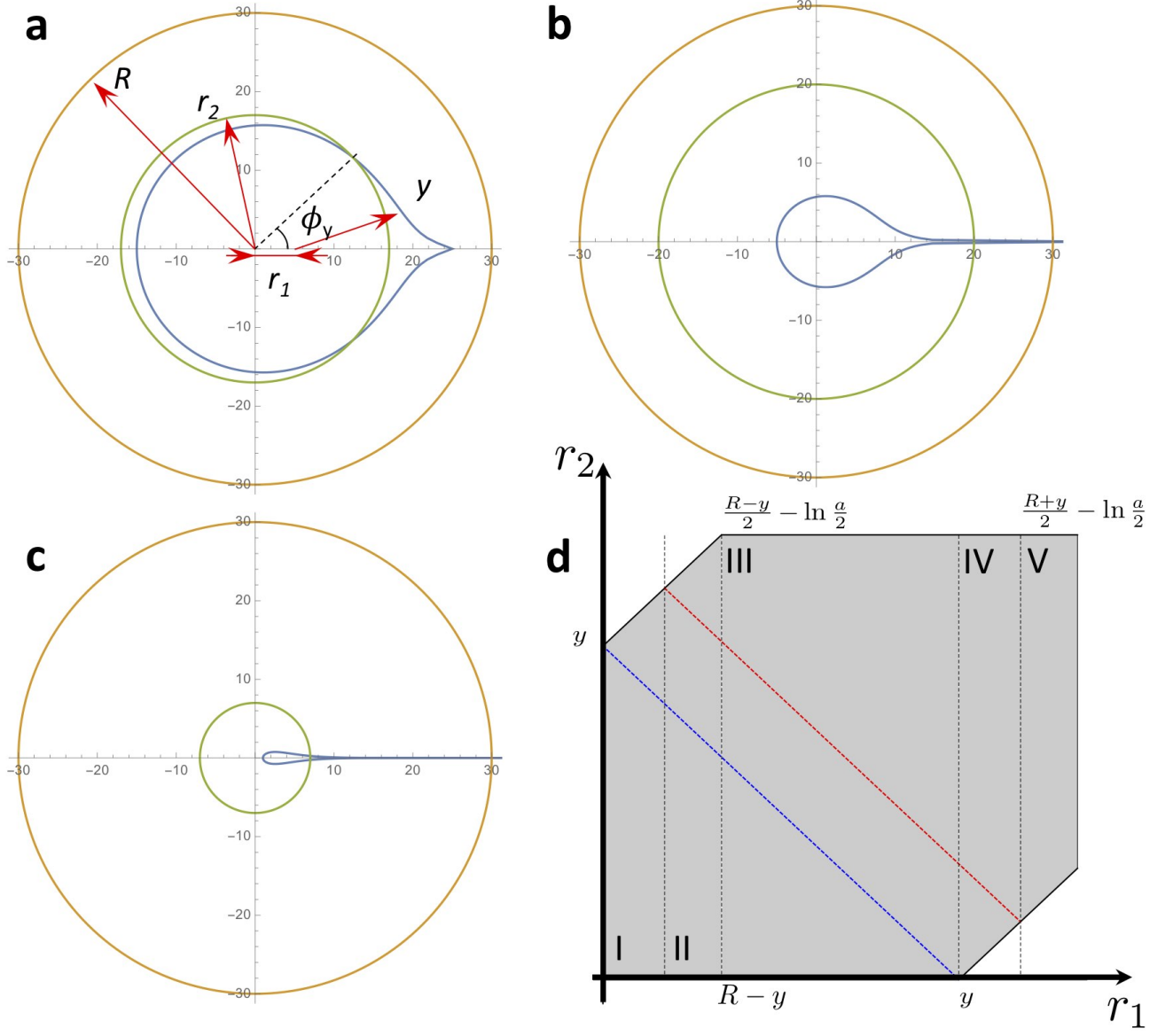


FIG. 13: **Integration domain for $\bar{k}_y(a)$ in the case $y < R$.** The integration is performed at the intersection of two hyperbolic disks. The first disk (yellow) corresponds to the latent space of the HRG, has radius R and is centered at the origin. The second disk (blue) has radius y and is centered at $(r_1, 0)$. The third disk depicts the integration radius r_2 that sweeps the integration domain. Angle $\phi_y \approx 2e^{y-r_1-r_2}$ corresponds to the intersection of disks y and r_2 . Based on R , y , and r_1 values we distinguish three configurations. **a**, Disk y contains the origin and is fully contained within R , regions I and II. **b**, Disk y contains the origin and is partially contained within R , region III. **c**, Disk y does not contain the origin and is partially contained within R , regions IV and V. **d**, Shaded region corresponds to the integration domain for $\bar{k}_y(a)$. Vertical dashed lines separate the five integration regions. Phase space below the blue dashed lines corresponds to the case of disk r_2 fully contained within disk y . Phase space above the blue line corresponds to the case of disk r_2 intersecting disk y . The red dashed line is given by $r_2 + r_1 = R - 2 \ln(\frac{a}{2})$ and corresponds to the loci of the integrand maxima in regions, II, III, and IV.

where $\bar{k}_y(r|a)$ is the average degree of node with radial coordinate r in noisy subgraph $G_y(a)$:

$$\bar{k}_y(r_1|a) = \frac{N}{(2\pi)} \int \cdots \int_{x(r_1, r_2, \hat{\phi}) \leq y} dr_2 \rho(r_2) d\hat{\phi} d\hat{\rho}(\hat{\phi}|\hat{\phi}) p[x(r_1, r_2, \hat{\phi})], \quad (\text{D22})$$

and angles $\phi \equiv \Delta\theta_{12}$ and $\hat{\phi} \equiv \Delta\hat{\theta}_{12}$ are introduced to ease the notation.

To evaluate $\bar{k}_y(r_1|a)$ we note that the integration region in Eq. (D22) is given by intersection of two hyperbolic

disks. The first one is of radius R and is centered at the coordinate system origin, $(0, 0)$. The second disk is of radius y and is centered at $(r_1, 0)$.

We perform the integration for the two regimes of $y \in [0, R]$ and $y \in [R, 2R]$ separately.

$$a. \quad y \in [0, R]$$

To evaluate $\bar{k}_y(r_1|a)$ for the $y \leq R$ case we need to distinguish five cases: (i) $0 \leq r_1 \leq \frac{R-y}{2} - \ln \frac{a}{2}$, (ii) $\frac{R-y}{2} - \ln \frac{a}{2} \leq r_1 \leq R-y$, (iii) $R-y \leq r_1 \leq y$, (iv) $y \leq r_1 \leq \frac{R+y}{2} - \ln \frac{a}{2}$, (v) $\frac{R+y}{2} - \ln \frac{a}{2} \leq r_1 \leq R$, which we depict for convenience in Fig. 13.

Region I: $0 \leq r_1 \leq \frac{R-y}{2} - \ln \frac{a}{2}$.

In this region the disk y is fully contained within the disk R . Further, since $y > R/2$, disk y is guaranteed to include the coordinate system origin for all $r_1 \in [0, R-y]$ values, Fig. 13a. In this case the integral in $\bar{k}_y(r_1|a)$ can be evaluated as

$$\bar{k}_y(r_1|a) = \mathfrak{I}_1 + \mathfrak{I}_2, \quad (\text{D23})$$

$$\mathfrak{I}_1 = \frac{N}{2\pi} \int_0^{y-r_1} dr_2 \rho(r_2) \int_0^{2\pi} d\hat{\phi} \int_{\hat{\phi}-a}^{\hat{\phi}+a} d\phi \tilde{\rho}(\phi|\hat{\phi}) p[x(r_1, r_2, \phi)], \quad (\text{D24})$$

$$\mathfrak{I}_2 = \frac{N}{\pi} \int_{y-r_1}^{y+r_1} dr_2 \rho(r_2) \int_0^{\phi_y} d\hat{\phi} \int_{\hat{\phi}-a}^{\hat{\phi}+a} d\phi \tilde{\rho}(\phi|\hat{\phi}) p[x(r_1, r_2, \phi)], \quad (\text{D25})$$

where ϕ_y is the angle given by the intersection of disk with radius r_2 centered at $r = 0$ and that of radius y , centered at $r = r_1$. To estimate ϕ_y we consider the triangle formed by the origin $(0, 0)$, disk y center at $(r_1, 0)$ and the intersection of r_2 with y . The triangle has sides equal r_1 , r_2 and y with ϕ_y being the angle between r_1 and r_2 . Thus, ϕ_y is given by the hyperbolic law of cosines:

$$\cosh y = \cosh r_1 \cosh r_2 - \sinh r_1 \sinh r_2 \cos \phi_y, \quad (\text{D26})$$

In the case of sufficiently large r_1 , r_2 , and y values we can approximate $\cos \phi_y$ as

$$\cos \phi_y \approx 1 - 2e^{y-r_1-r_2} \quad (\text{D27})$$

Since $\hat{\phi}$ in the first integral sweeps the entire 2π angle, \mathfrak{I}_1 is given by

$$\mathfrak{I}_1 = \frac{N}{2\pi} \int_0^{y-r_1} dr_2 \rho(r_2) \int_0^{2\pi} d\hat{\phi} p[x(r_1, r_2, \hat{\phi})] \quad (\text{D28})$$

Then, since $x(r_1, r_2, \hat{\phi}) \leq r_1 + r_2 \leq R$, $p[x(r_1, r_2, \hat{\phi})] \approx 1$, leading to

$$\mathfrak{I}_1 = Ne^{\alpha(y-r_1-R)}, \quad (\text{D29})$$

The evaluation of \mathfrak{I}_2 is more involved and requires further approximations. We notice that $\phi_y \ll 1$ since $r_2 \in [y-r_1, y+r_1]$, and can be further approximated as

$$\phi_y \approx 2e^{\frac{y-r_1-r_2}{2}}. \quad (\text{D30})$$

Then, for sufficiently large noise amplitudes $a \gg \phi_y$, we can approximate the integral $\int_{\hat{\phi}-a}^{\hat{\phi}+a} d\phi$ as $2 \int_0^a d\phi$, resulting in

$$\mathfrak{I}_2 = \frac{2N}{\pi a^2} \int_{y-r_1}^{y+r_1} dr_2 \rho(r_2) \phi_y \int_0^a \frac{d\phi (a-\phi)}{1 + \exp\left(\frac{x(r_1, r_2, \phi)-R}{2T}\right)} \quad (\text{D31})$$

Since $r_1 < \frac{R-y}{2} - \ln \frac{a}{2}$, $r_2 < y+r_1$, and $y < R$, it follows that $x(r_1, r_2, \phi) < r_1 + r_2 + 2 \ln \frac{a}{2} < R$, and, as a result, $\exp\left(\frac{x(r_1, r_2, \phi)-R}{2T}\right) \ll 1$, resulting in

$$\mathfrak{I}_2 = \frac{4\alpha N}{\pi(2\alpha-1)} e^{-\alpha R} e^{\alpha y} e^{(\alpha-1)r_1}. \quad (\text{D32})$$

We are primarily interested in the $\gamma > 2$ case, which corresponds to $\alpha > 1/2$. In this case $\mathfrak{I}_2 \gg \mathfrak{I}_1$, and

$$\bar{k}_y(r_1|a) \approx \mathfrak{I}_2 = \frac{4\alpha N}{\pi(2\alpha-1)} e^{-\alpha R} e^{\alpha y} e^{(\alpha-1)r_1}. \quad (\text{D33})$$

Region II: $\frac{R-y}{2} - \ln \frac{a}{2} \leq r_1 \leq R-y$.

Similar to Region I, the hyperbolic disk y fully lies within disk R , Fig. 13a. Thus, $\bar{k}_y(r_1|a)$ is given by the same expression

$$\bar{k}_y(r_1|a) = \mathfrak{I}_3 + \mathfrak{I}_4, \quad (\text{D34})$$

$$\mathfrak{I}_3 = \frac{N}{2\pi} \int_0^{y-r_1} dr_2 \rho(r_2) \int_0^{2\pi} d\hat{\phi} \int_{\hat{\phi}-a}^{\hat{\phi}+a} d\phi \tilde{\rho}(\phi|\hat{\phi}) p[x(r_1, r_2, \phi)], \quad (\text{D35})$$

$$\mathfrak{I}_4 = \frac{N}{\pi} \int_{y-r_1}^{y+r_1} dr_2 \rho(r_2) \int_0^{\phi_y} d\hat{\phi} \int_{\hat{\phi}-a}^{\hat{\phi}+a} d\phi \tilde{\rho}(\phi|\hat{\phi}) p[x(r_1, r_2, \phi)]. \quad (\text{D36})$$

The calculation of \mathfrak{I}_3 is identical to that of \mathfrak{I}_1 , resulting in

$$\mathfrak{I}_3 = \mathfrak{I}_1 = N e^{\alpha(y-r_1-R)}. \quad (\text{D37})$$

Different from region I is the calculation of \mathfrak{I}_4 . Indeed, in the case $r_1 \geq \frac{R-y}{2} + \ln \frac{a}{2}$, and $r_2 \in [y-r_1, y+r_1]$ hyperbolic distance $x(r_1, r_2, \phi)$ is no longer guaranteed to be smaller than R , and $p[x(r_1, r_2, \phi)]$ can no longer be approximated by unity. We first split \mathfrak{I}_4 into two parts and calculate them separately:

$$\mathfrak{I}_4 = \mathfrak{I}_{41} - \mathfrak{I}_{42}, \quad (\text{D38})$$

where

$$\mathfrak{I}_{41} = \frac{N}{\pi a} \int_{y-r_1}^{y+r_1} dr_2 \rho(r_2) \phi_y \int_0^a \frac{d\phi}{1 + \exp\left(\frac{x(r_1, r_2, \phi) - R}{2T}\right)}, \quad (\text{D39})$$

$$\mathfrak{I}_{42} = \frac{N}{\pi a^2} \int_{y-r_1}^{y+r_1} dr_2 \rho(r_2) \phi_y \int_0^a \frac{\phi d\phi}{1 + \exp\left(\frac{x(r_1, r_2, \phi) - R}{2T}\right)}, \quad (\text{D40})$$

$$(\text{D41})$$

By approximating the hyperbolic law of cosines in Eq. (3) as, $x(r_1, r_2, \phi) \approx r_1 + r_2 + 2 \ln \frac{\phi}{2}$ and making use of Eq. (D30) we obtain for \mathfrak{I}_{41} :

$$\mathfrak{I}_{41} = \frac{4\alpha N}{\pi a} e^{\left(\frac{1}{2}-\alpha\right)R} e^{\frac{y}{2}} e^{-r_1} \int_{y-r_1}^{y+r_1} dr_2 e^{(\alpha-1)r_2} I\left(\frac{a}{2} e^{\frac{r_1+r_2-R}{2}}; T\right), \quad (\text{D42})$$

where $I(z; T) \equiv \int_0^z \frac{dx}{1+x^{\frac{1}{T}}}$ is the same function as in Eq. (27).

Recall that for small $z \ll 1$ function $I(z; T) \approx z$, while for $z \gg 1$, $I(z; T) \approx I(T) = \frac{\pi}{T \sin(\frac{\pi}{T})}$. With these approximations in mind we split the integration in \mathfrak{I}_{41} into two subregions :

$$\int_{y-r_1}^{y+r_1} dr_2 = \int_{y-r_1}^{R-r_1-2 \ln \frac{a}{2}} dr_2 + \int_{R-r_1-2 \ln \frac{a}{2}}^{y+r_1} dr_2 \quad (\text{D43})$$

In the first subregion, $r_2 \in [y-r_1, R-r_1-2 \ln \frac{a}{2}]$, and $\frac{a}{2} e^{\frac{r_1+r_2-R}{2}} \leq 1$, which allows us to approximate $I\left(\frac{a}{2} e^{\frac{r_1+r_2-R}{2}}; T\right) \approx \frac{a}{2} e^{\frac{r_1+r_2-R}{2}}$. In the second subregion, $r_2 \in [R-r_1-2 \ln \frac{a}{2}, y+r_1]$, $\frac{a}{2} e^{\frac{r_1+r_2-R}{2}} \geq 1$, and $I\left(\frac{a}{2} e^{\frac{r_1+r_2-R}{2}}; T\right) \approx I(T)$. Using these approximations we obtain, to the leading order

$$\mathfrak{I}_{41} = \frac{4N\alpha}{\pi} \left[\frac{1}{2\alpha-1} + \frac{I(T)}{1-\alpha} \right] e^{\frac{y-R}{2}} e^{-\alpha r_1} \left(\frac{a}{2}\right)^{1-2\alpha}. \quad (\text{D44})$$

Following the same approximation steps,

$$\mathfrak{J}_{42} = \frac{2N\alpha}{\pi} \left[\frac{1}{2\alpha - 1} + \frac{8\tilde{I}(T)}{3 - 2\alpha} \right] e^{\frac{y-R}{2}} e^{-\alpha r_1} \left(\frac{a}{2} \right)^{1-2\alpha} \quad (\text{D45})$$

where

$$\tilde{I}(T) \equiv \int_0^\infty \frac{x dx}{1 + x^{\frac{1}{T}}} = \frac{\pi T}{\sin(2\pi T)} \quad (\text{D46})$$

in the case $T < 1/2$.

Taken together, \mathfrak{J}_{41} and \mathfrak{J}_{42} result in

$$\mathfrak{J}_4 = \frac{2N\alpha}{\pi} \left[\frac{1}{2\alpha - 1} + \frac{2I(T)}{1 - \alpha} - \frac{8\tilde{I}(T)}{3 - 2\alpha} \right] e^{\frac{y-R}{2}} e^{-\alpha r_1} \left(\frac{a}{2} \right)^{1-2\alpha}. \quad (\text{D47})$$

Finally, since $y < R$, we conclude that $\mathfrak{J}_3 \ll \mathfrak{J}_4$, resulting in

$$\bar{k}_y(r_1|a) \approx \frac{2N\alpha}{\pi} \left[\frac{1}{2\alpha - 1} + \frac{2I(T)}{1 - \alpha} - \frac{8\tilde{I}(T)}{3 - 2\alpha} \right] e^{\frac{y-R}{2}} e^{-\alpha r_1} \left(\frac{a}{2} \right)^{1-2\alpha} \quad (\text{D48})$$

for $\frac{R-y}{2} - \ln \frac{a}{2} \leq r_1 \leq R - y$.

Region III: $R - y \leq r_1 \leq y$.

In this region disk y is partially contained within the disk R . Since $r_1 \leq y$, disk y still contains the coordinate system origin, Fig. 13b. Similar to regions I and II, we split the calculation of $\bar{k}_y(r_1|a)$ into two parts:

$$\bar{k}_y(r_1|a) = \mathfrak{J}_5 + \mathfrak{J}_6, \quad (\text{D49})$$

$$\mathfrak{J}_5 = \frac{N}{2\pi} \int_0^{y-r_1} dr_2 \rho(r_2) \int_0^{2\pi} d\hat{\phi} \int_{\hat{\phi}-a}^{\hat{\phi}+a} d\phi \tilde{\rho}(\phi|\hat{\phi}) p[x(r_1, r_2, \phi)], \quad (\text{D50})$$

$$\mathfrak{J}_6 = \frac{N}{\pi} \int_{y-r_1}^R dr_2 \rho(r_2) \int_0^{\phi_y} d\hat{\phi} \int_{\hat{\phi}-a}^{\hat{\phi}+a} d\phi \tilde{\rho}(\phi|\hat{\phi}) p[x(r_1, r_2, \phi)], \quad (\text{D51})$$

where $\phi_y \ll 1$ is the intersection angle of disk r_2 with that of y , see Fig. 13b, and is given by Eq. (D30).

We first note that the integral in \mathfrak{J}_5 is identical to those in \mathfrak{J}_3 and \mathfrak{J}_1 :

$$\mathfrak{J}_5 = \mathfrak{J}_1 = N e^{\alpha(y-r_1-R)}. \quad (\text{D52})$$

The integration in \mathfrak{J}_6 is very similar to that in \mathfrak{J}_4 with the only difference in the upper integration bound of $r_2 \leq R$. The evaluation of \mathfrak{J}_6 is, therefore, is straightforward and requires the same approximation steps as in \mathfrak{J}_4 . A quicker estimate can be obtained by noting that the upper bound for r_2 in \mathfrak{J}_4 does not contribute to the leading term. The reason is that \mathfrak{J}_{42} is dominated by r_2 in the vicinity of the $r_2 = R - r_1 - 2 \ln \frac{a}{2}$ point.

Since $R > R - r_1 - 2 \ln \frac{a}{2}$

$$\mathfrak{J}_6 = \int_{y-r_1}^{R-r_1-2 \ln \frac{a}{2}} dr_2 + \int_{R-r_1-2 \ln \frac{a}{2}}^R dr_2 \quad (\text{D53})$$

with integrands identical to those of \mathfrak{J}_{41} and \mathfrak{J}_{42} . Since the integrand in \mathfrak{J}_{42} is dominated by smaller r_2 values we conclude that

$$\mathfrak{J}_6 = \mathfrak{J}_4 \quad (\text{D54})$$

Finally, \mathfrak{J}_6 dominates \mathfrak{J}_5 for $\alpha > \frac{1}{2}$, resulting in

$$\bar{k}_y(r_1|a) \approx \frac{2N\alpha}{\pi} \left[\frac{1}{2\alpha - 1} + \frac{2I(T)}{1 - \alpha} - \frac{8\tilde{I}(T)}{3 - 2\alpha} \right] e^{\frac{y-R}{2}} e^{-\alpha r_1} \left(\frac{a}{2} \right)^{1-2\alpha} \quad (\text{D55})$$

for $R - y \leq r_1 \leq y$.

Region IV: $y \leq r_1 \leq \frac{R+y}{2} - \ln \frac{a}{2}$.

In this region, hyperbolic disk y is partially contained within R and does not include the origin, Fig. 13c. Therefore, in this region

$$\bar{k}_y(r_1|a) = \frac{N}{\pi} \int_{r_1-y}^R dr_2 \rho(r_2) \int_0^{\phi_y} d\hat{\phi} \int_{\hat{\phi}-a}^{\hat{\phi}+a} d\phi \tilde{\rho}(\phi|\hat{\phi}) p[x(r_1, r_2, \phi)], \quad (\text{D56})$$

Using the arguments similar to that of Region III, we obtain:

$$\bar{k}_y(r_1|a) \approx \frac{2N\alpha}{\pi} \left[\frac{1}{2\alpha-1} + \frac{2I(T)}{1-\alpha} - \frac{8\tilde{I}(T)}{3-2\alpha} \right] e^{\frac{y-R}{2}} e^{-\alpha r_1} \left(\frac{a}{2} \right)^{1-2\alpha} \quad (\text{D57})$$

for $y \leq r_1 \leq \frac{R+y}{2} - \ln \frac{a}{2}$.

Region V: $\frac{R+y}{2} - \ln \frac{a}{2} \leq r_1 \leq R$.

Similar to the situation in region IV, hyperbolic disk y intersects disk R and does not include the coordinate system origin. Different from region IV is the $r_2 = R - r_1 - 2 \ln \frac{a}{2}$ point that lies outside the r_2 integration region and we can no longer relate $\bar{k}_y(r_1|a)$ to those in other regions.

To evaluate

$$\bar{k}_y(r_1|a) = \frac{N}{\pi} \int_{r_1-y}^R dr_2 \rho(r_2) \int_0^{\phi_y} d\hat{\phi} \int_{\hat{\phi}-a}^{\hat{\phi}+a} d\phi \tilde{\rho}(\phi|\hat{\phi}) p[x(r_1, r_2, \phi)] \quad (\text{D58})$$

we recall that $\phi_y \ll 1$, and for sufficiently large $a \gg \phi_y$ we obtain

$$\bar{k}_y(r_1|a) = \mathfrak{I}_7 - \mathfrak{I}_8, \quad (\text{D59})$$

$$\mathfrak{I}_7 = \frac{N}{\pi a} \int_{r_1-y}^R dr_2 \rho(r_2) \phi_y \int_0^a \frac{d\phi}{1 + \exp\left(\frac{x(r_1, r_2, \phi) - R}{2T}\right)}, \quad (\text{D60})$$

$$\mathfrak{I}_8 = \frac{N}{\pi a^2} \int_{r_1-y}^R dr_2 \rho(r_2) \phi_y \int_0^a \frac{\phi d\phi}{1 + \exp\left(\frac{x(r_1, r_2, \phi) - R}{2T}\right)}, \quad (\text{D61})$$

After straightforward approximations we obtain

$$\bar{k}_y(r_1|a) = \frac{4\alpha N}{\pi a} e^{(\frac{1}{2}-\alpha)R} e^{(\frac{3}{2}-\alpha)y} e^{(\alpha-2)r_1} \left[\frac{I(T)}{1-\alpha} - \frac{4\tilde{I}(T)}{a(3-2\alpha)} e^{\frac{R+y}{2}-r_1} \right] \quad (\text{D62})$$

for $\frac{R+y}{2} - \ln \frac{a}{2} \leq r_1 \leq R$

Merged together, Eqs. (D33), (D48), (D55), (D57), and (D62) provide the solution for $\bar{k}_y(r_1|a)$:

$$\bar{k}_y(r_1|a) \approx \begin{cases} \frac{4\alpha N}{\pi(2\alpha-1)} e^{-\alpha R} e^{\alpha y} e^{(\alpha-1)r_1} & \text{if } 0 \leq r_1 \leq \frac{R+y}{2} - \ln \frac{a}{2}, \\ \frac{2N\alpha}{\pi} \left[\frac{1}{2\alpha-1} + \frac{2I(T)}{1-\alpha} - \frac{8\tilde{I}(T)}{3-2\alpha} \right] e^{\frac{y-R}{2}} e^{-\alpha r_1} \left(\frac{a}{2} \right)^{1-2\alpha} & \text{if } \frac{R+y}{2} - \ln \frac{a}{2} \leq r_1 \leq \frac{R+y}{2} - \ln \frac{a}{2}, \\ \frac{4\alpha N}{\pi a} e^{(\frac{1}{2}-\alpha)R} e^{(\frac{3}{2}-\alpha)y} e^{(\alpha-2)r_1} \left[\frac{I(T)}{1-\alpha} - \frac{4\tilde{I}(T)}{a(3-2\alpha)} e^{\frac{R+y}{2}-r_1} \right] & \text{if } \frac{R+y}{2} - \ln \frac{a}{2} \leq r_1 \leq R. \end{cases} \quad (\text{D63})$$

Using Eq. (D63) together with Eq. (D21) we finally obtain

$$k_y(a) \sim N e^{-(\alpha+\frac{1}{2})R} e^{\frac{y}{2}} a^{1-2\alpha}, \quad (\text{D64})$$

$$b. \quad y \in [R, 2R]$$

In the regime $y \geq R$ hyperbolic disk y always contains the origin, Fig. 14. To evaluate $\bar{k}_y(r_1|a)$ in this regime we need distinguish 2 cases, (VI) $0 \leq r_1 \leq y - R$, and (VII) $y - R \leq r_1, R$.

Region VI: $0 \leq r_1 \leq y - R$.

In this regime hyperbolic disk R is fully contained within hyperbolic disk y , Fig. 14a, and the $\bar{k}_y(r_1|a) = \bar{k}(r_1)$, where $\bar{k}(r_1)$ is the average degree of a node at r_1 in the HRG graph. Indeed, radial coordinates of all points are

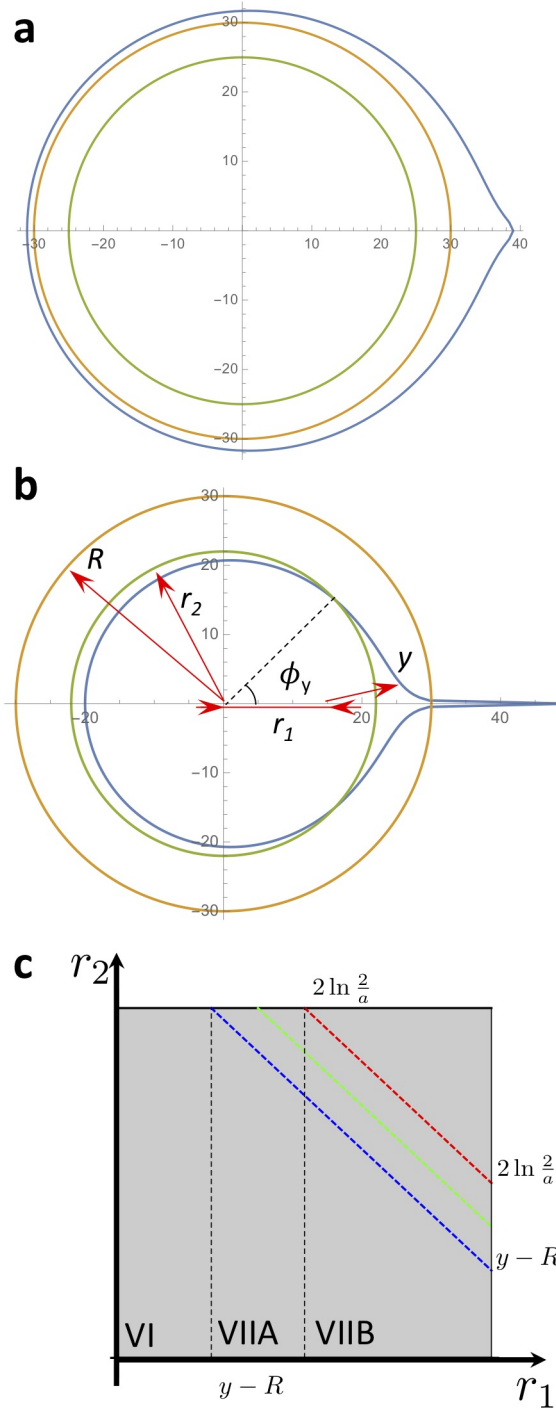


FIG. 14: **Integration domain for $\bar{k}_y(a)$ at $y > R$.** The integration is performed at the intersection of two hyperbolic disks. The first disk (yellow) corresponds to the latent space of the HRG, has radius R and is centered at the origin. The second disk (blue) has radius y and is centered at $(r_1, 0)$. The third disk (green) depicts the integration radius r_2 that sweeps the integration domain. Angle ϕ_y corresponds to the intersection of disks y and r_2 . Based on R , y , and r_1 values, we distinguish two configurations. **a**, Disk y fully contains disk R , regions VI. **b**, Disk y overlaps within R , region VII. **c**, The integration domain $\bar{k}_y(a)$ is shown by the shaded region. Vertical dashed lines separate the domain into two integration regions, VI and VII. Region VII further splits into subregions VIIA and VIIB. Phase space below the blue dashed line corresponds to the case of disk r_2 fully contained within disks y and R . Phase space above the blue line corresponds to the case of disk r_2 intersecting disk y . The red dashed line is given by $r_2 + r_1 = R - 2 \ln \frac{2}{a}$ and corresponds to the loci of the integrand maxima in region VII. Green dashed line corresponds to the $\tilde{R}(r_1)$ line. By construction, $\phi_y \ll 1$ for $r_2 \geq \tilde{R}(r_1)$.

within disk R , and all distances from point $(r_1, 0)$ to any point within disk R are guaranteed to be smaller than y , $x(r_1, 0, r_2, \theta) < y$ for any $\theta \in [0, 2\pi]$. Therefore in this regime

$$\bar{k}_y(r_1|a) = \frac{N}{2\pi} \int_0^R dr_2 \rho(r_2) \int_0^{2\pi} d\hat{\phi} \int_{\hat{\phi}-a}^{\hat{\phi}+a} d\phi \tilde{\rho}(\phi|\hat{\phi}) p[x(r_1, r_2, \phi)], \quad (\text{D65})$$

Since the integral over $\hat{\phi}$ sweeps the entire circle, $\hat{\theta} \in [0, 2\pi]$, synthetic noise does not affect the integration:

$$\bar{k}_y(r_1|a) = \frac{N}{2\pi} \int_0^R dr_2 \rho(r_2) \int_0^{2\pi} d\phi p[x(r_1, r_2, \phi)] = \bar{k}(r_1), \quad (\text{D66})$$

resulting in

$$\bar{k}_y(r_1|a) = \frac{4\alpha N I(T)}{(2\alpha - 1)\pi} e^{-\frac{r_1}{2}} \quad (\text{D67})$$

in the case $0 \leq r_1 \leq y - R$.

Region VII: $R - y \leq r_1 \leq R$. In this regime hyperbolic disk R is partially contained within y and the calculation of $\bar{k}_y(r_1|a)$ splits into two integrals,

$$\bar{k}_y(r_1|a) = \mathfrak{I}_9 + \mathfrak{I}_{10}, \quad (\text{D68})$$

$$\mathfrak{I}_9 = \frac{N}{2\pi} \int_0^{y-r_1} dr_2 \rho(r_2) \int_0^{2\pi} d\phi p[x(r_1, r_2, \phi)] = \bar{k}(r_1), \quad (\text{D69})$$

$$\mathfrak{I}_{10} = \frac{N}{\pi} \int_{y-r_1}^R dr_2 \rho(r_2) \int_0^{\phi_y} d\hat{\phi} \int_{\hat{\phi}-a}^{\hat{\phi}+a} d\phi \tilde{\rho}(\phi|\hat{\phi}) p[x(r_1, r_2, \phi)], \quad (\text{D70})$$

where ϕ_y is the angle of intersection of disks R and y , Fig. 14b.

We note that the integration region for \mathfrak{I}_9 is identical to that of \mathfrak{I}_1 . Different, from the case of \mathfrak{I}_1 is the condition that $y > R$. In this case $x(r_1, r_2, \phi)$ is no longer guaranteed to be less than R , and $p[x(r_1, r_2, \phi)]$ cannot be approximated by 1. We start evaluating \mathfrak{I}_9 by performing the integration over ϕ , which leads to

$$\mathfrak{I}_9 = \frac{2\alpha N}{\pi} e^{-(\alpha-\frac{1}{2})R} e^{-\frac{r_1}{2}} \int_0^{y-r_1} dr_2 e^{(\alpha-\frac{1}{2})r_2} I\left(\frac{\pi}{2} e^{\frac{r_1+r_2-R}{2}}; T\right), \quad (\text{D71})$$

where $I(z; T)$ is given by Eq. (27). Recall that $I(z; T) \approx z$ if $z \ll 1$ and $I(z; T) \approx I(\infty; T)$ in case $z \gg 1$. Thus, to evaluate \mathfrak{I}_9 we split the integration over r_2 in to two integrals, $\int_0^{y-r_1} = \int_0^{R-r_1-2\ln\frac{\pi}{2}} + \int_{R-r_1-2\ln\frac{\pi}{2}}^{y-r_1}$. In the first integral $\frac{\pi}{2} e^{\frac{r_1+r_2-R}{2}} < 1$ and we approximate $I\left(\frac{\pi}{2} e^{\frac{r_1+r_2-R}{2}}; T\right) \approx \frac{\pi}{2} e^{\frac{r_1+r_2-R}{2}}$, while in the second integral $\frac{\pi}{2} e^{\frac{r_1+r_2-R}{2}} > 1$ and $I\left(\frac{\pi}{2} e^{\frac{r_1+r_2-R}{2}}; T\right) \approx I(\infty; T)$. The remaining integration steps in \mathfrak{I}_9 are straightforward, resulting in

$$\mathfrak{I}_9 \approx \frac{2\alpha N}{\pi} e^{-(\alpha-\frac{1}{2})R} e^{-\alpha r_1} \left[\frac{1}{\alpha} \left(\frac{\pi}{2}\right)^{1-2\alpha} e^{R(\alpha-\frac{1}{2})} + \frac{2I(\infty; T)}{2\alpha-1} e^{y(\alpha-\frac{1}{2})} \right]. \quad (\text{D72})$$

Finally, since $y > R$ and $\alpha > \frac{1}{2}$, we get

$$\mathfrak{I}_9 \approx \frac{4\alpha I(\infty; T) N}{(2\alpha-1)\pi} e^{(\alpha-\frac{1}{2})(y-R)} e^{-\alpha r_1}. \quad (\text{D73})$$

In order to calculate \mathfrak{I}_{10} we first need to estimate the cutoff angle ϕ_y , which is given by the intersection of disks R and y , and is given by Eq. (D27). ϕ_y takes values from $\phi_y \approx 2e^{\frac{y-2R}{2}}$ at $r_1 = r_2 = R$ to $\phi_y = \pi$ at $r_2 = y - r_1$. Thus, we can no longer use the $\phi_y \ll a$ approximation, as in \mathfrak{I}_2 .

To proceed further we note that the integration domain in \mathfrak{I}_{10} is given by the area above the $r_2 = y - r_1$ line, Fig. 14c. We recall that the integration in the case $y < R$ is dominated by points in the vicinity of the $r_1 + r_2 = R - 2\ln\frac{a}{2}$ line, see red dashed line in Fig. 13c. Let us assume that this is also the case in the $y \geq R$ regime, red dashed line in Fig. 14c. We next note that in the vicinity of $r_1 + r_2 = R - 2\ln\frac{a}{2}$ line $\cos\phi_y \approx 1 - 2e^{y-R-2\ln\frac{a}{2}}$. For sufficiently small noise amplitude, such that $y < R - 2\ln\frac{a}{2}$, the cutoff angle $\phi_y \ll 1$ and can be approximated by Eq. (D30), and we can employ the same approximation techniques as in \mathfrak{I}_2 .

Our strategy now is to split the integration domain of \mathfrak{I}_{10} into two parts by curve $r_2 = \tilde{R}(r_1)$ such that (i) this curve is below the $r_1 + r_2 = R - 2 \ln \frac{a}{2}$ line, and (ii) above this curve, $r_2 > \tilde{R}(r_1)$, the cutoff angle $\phi_y \ll 1$. One possibility for such curve is $\tilde{R}(r_1) = A - r_1$ line, where $A = \frac{y+R}{2} - \ln \frac{a}{2}$, green dashed curve in Fig. 14c.

Then region VII splits into two subregions, VIIA and VIIB, corresponding to $r_1 \in [y - R, 2 \ln \frac{a}{2}]$ and $r_1 \in [2 \ln \frac{a}{2}, R]$, respectively, see Fig. 14c. We expect that the contribution to $k_y(a)$ from VIIA to be much small than that from VIIB since the latter contains $r_1 + r_2 = R - 2 \ln \frac{a}{2}$ line and the former does not. Therefore, we will estimate the upper bound for $k_y(r_1|a)$ in VIIA by replacing ϕ_y with π . In subregion VIIB we split the integration over r_2 into two intervals, $r_2 \in [0, \tilde{R}(r_1)]$ and $r_2 \in [\tilde{R}(r_1), R]$.

Subregion VIIA: $y - R \leq r_1 \leq 2 \ln \frac{a}{2}$.

Here the integral splits into

$$\bar{k}_y(r_1|a) = \mathfrak{I}_{11} + \mathfrak{I}_{12}, \quad (\text{D74})$$

$$\mathfrak{I}_{11} = \frac{N}{2\pi} \int_0^{y-r_1} dr_2 \rho(r_2) \int_0^{2\pi} d\phi p[x(r_1, r_2, \phi)] = \bar{k}(r_1), \quad (\text{D75})$$

$$\mathfrak{I}_{12} = \frac{N}{\pi} \int_{y-r_1}^R dr_2 \rho(r_2) \int_0^{\phi_y} d\hat{\phi} \int_{\hat{\phi}-a}^{\hat{\phi}+a} d\phi \tilde{\rho}(\phi|\hat{\phi}) p[x(r_1, r_2, \phi)], \quad (\text{D76})$$

Following our strategy, we evaluate the upper bound for \mathfrak{I}_{12} by replacing the integration limit of ϕ_y with π :

$$\mathfrak{I}_{12} \leq \frac{N}{\pi} \int_{y-r_1}^R dr_2 \rho(r_2) \int_0^\pi d\hat{\phi} \int_{\hat{\phi}-a}^{\hat{\phi}+a} d\phi \tilde{\rho}(\phi|\hat{\phi}) p[x(r_1, r_2, \phi)]. \quad (\text{D77})$$

Then,

$$\bar{k}_y(r_1|a) \leq \bar{k}(r_1) = \frac{4\alpha N I(\infty; T)}{(2\alpha - 1)\pi} e^{-\frac{r_1}{2}} \quad (\text{D78})$$

for $y - R \leq r_1 \leq 2 \ln \frac{a}{2}$.

Region VIIB: $2 \ln \frac{a}{2} \leq r_1 \leq R$.

Here we distinguish three intervals:

$$\bar{k}_y(r_1|a) = \mathfrak{I}_{13} + \mathfrak{I}_{14} + \mathfrak{I}_{15}, \quad (\text{D79})$$

$$\mathfrak{I}_{13} = \frac{N}{2\pi} \int_0^{y-r_1} dr_2 \rho(r_2) \int_0^{2\pi} d\phi p[x(r_1, r_2, \phi)], \quad (\text{D80})$$

$$\mathfrak{I}_{14} = \frac{N}{\pi} \int_{y-r_1}^{\tilde{R}(r_1)} dr_2 \rho(r_2) \int_0^{\phi_y} d\hat{\phi} \int_{\hat{\phi}-a}^{\hat{\phi}+a} d\phi \tilde{\rho}(\phi|\hat{\phi}) p[x(r_1, r_2, \phi)], \quad (\text{D81})$$

$$\mathfrak{I}_{15} = \frac{N}{\pi} \int_{\tilde{R}(r_1)}^R dr_2 \rho(r_2) \int_0^{\phi_y} d\hat{\phi} \int_{\hat{\phi}-a}^{\hat{\phi}+a} d\phi \tilde{\rho}(\phi|\hat{\phi}) p[x(r_1, r_2, \phi)], \quad (\text{D82})$$

$$(\text{D83})$$

where $\tilde{R}(r_1) = \frac{y+R}{2} - \ln \frac{a}{2} - r_1$.

We evaluate the upper bound for \mathfrak{I}_{14} by replacing the ϕ_y cutoff with π

$$\mathfrak{I}_{14} \leq \frac{N}{2\pi} \int_{y-r_1}^{\tilde{R}(r_1)} dr_2 \rho(r_2) \int_0^{2\pi} d\hat{\phi} \int_{\hat{\phi}-a}^{\hat{\phi}+a} d\phi \tilde{\rho}(\phi|\hat{\phi}) p[x(r_1, r_2, \phi)], \quad (\text{D84})$$

leading to

$$\mathfrak{I}_{13} + \mathfrak{I}_{14} \leq \frac{N}{2\pi} \int_0^{\tilde{R}(r_1)} dr_2 \rho(r_2) \int_0^{2\pi} d\phi p[x(r_1, r_2, \phi)]. \quad (\text{D85})$$

After the same calculation steps as in \mathfrak{I}_9 we obtain

$$\mathfrak{I}_{13} + \mathfrak{I}_{14} \leq \frac{4\alpha I(T)N}{(2\alpha - 1)\pi} e^{(\alpha - \frac{1}{2})(\tilde{R}(r_1) - R)} e^{-\alpha r_1}. \quad (\text{D86})$$

To evaluate \mathfrak{J}_{15} we use the $\phi_y \ll 1$ assumption, which enables us to use Eq. (D30). This approximation holds since $r_2 > \tilde{R}(r_1)$. Then, by following the same simplification steps as in \mathfrak{J}_4 we obtain

$$\mathfrak{J}_{15} = \mathfrak{J}_{151} - \mathfrak{J}_{152}, \quad (\text{D87})$$

$$\mathfrak{J}_{151} = \frac{N}{\pi a} \int_{\tilde{R}(r_1)}^R dr_2 \rho(r_2) \phi_y \int_0^a \frac{d\phi}{1 + \exp\left(\frac{x(r_1, r_2, \phi) - R}{2T}\right)}, \quad (\text{D88})$$

$$\mathfrak{J}_{152} = \frac{N}{\pi a^2} \int_{\tilde{R}(r_1)}^R dr_2 \rho(r_2) \phi_y \int_0^a \frac{\phi d\phi}{1 + \exp\left(\frac{x(r_1, r_2, \phi) - R}{2T}\right)}, \quad (\text{D89})$$

$$(\text{D90})$$

Following the same evaluation steps as in \mathfrak{J}_4 we confirm that both \mathfrak{J}_{151} and \mathfrak{J}_{152} are dominated by points in the vicinity of $r_1 + r_2 = R - 2 \ln \frac{a}{2}$, resulting in

$$\mathfrak{J}_{15} = \mathfrak{J}_4 = \frac{2N\alpha}{\pi} \left[\frac{1}{2\alpha - 1} + \frac{2I(T)}{1 - \alpha} - \frac{8\tilde{I}(T)}{3 - 2\alpha} \right] e^{\frac{y-R}{2}} e^{-\alpha r_1} \left(\frac{a}{2}\right)^{1-2\alpha}. \quad (\text{D91})$$

By comparing Eqs. (D91) and Eqs. (D86) we establish that $\mathfrak{J}_{15} \gg \mathfrak{J}_{13} + \mathfrak{J}_{14}$ since $R(\tilde{r}_1) < R$ and $y > R$, confirming our hypothesis and resulting in

$$\bar{k}_y(r_1|a) \approx \mathfrak{J}_4 = \frac{2N\alpha}{\pi} \left[\frac{1}{2\alpha - 1} + \frac{2I(T)}{1 - \alpha} - \frac{8\tilde{I}(T)}{3 - 2\alpha} \right] e^{\frac{y-R}{2}} e^{-\alpha r_1} \left(\frac{a}{2}\right)^{1-2\alpha} \quad (\text{D92})$$

in case $2 \ln \frac{a}{2} \leq r_1 \leq R$.

Taken together, our results for regions VI and VII read:

$$\bar{k}_y(r_1|a) \begin{cases} \approx \frac{4\alpha NI(\infty; T)}{\pi(2\alpha-1)} e^{-\frac{r_1}{2}} & \text{if } 0 \leq r_1 \leq y - R, \\ \leq \frac{4\alpha NI(\infty; T)}{(2\alpha-1)\pi} e^{-\frac{r_1}{2}} & \text{if } y - R \leq r_1 \leq 2 \ln \frac{a}{2}, \\ \approx \frac{2N\alpha}{\pi} \left[\frac{1}{2\alpha-1} + \frac{2I(T)}{1-\alpha} - \frac{8\tilde{I}(T)}{3-2\alpha} \right] e^{\frac{y-R}{2}} e^{-\alpha r_1} \left(\frac{a}{2}\right)^{1-2\alpha} & \text{if } 2 \ln \frac{a}{2} \leq r_1 \leq R. \end{cases} \quad (\text{D93})$$

Using Eq. (D93) together with Eq. (D21) we finally obtain

$$\bar{k}_y(a) = k_y^1(a) + k_y^2(a), \quad (\text{D94})$$

$$k_y^1(a) \leq \frac{8\alpha^2 NI(T)}{\pi(2\alpha-1)^2} e^{-\alpha R} \left(\frac{a}{2}\right)^{1-2\alpha}, \quad (\text{D95})$$

$$k_y^2(a) \approx \frac{2N\alpha^2}{\pi} \left[\frac{1}{2\alpha-1} + \frac{2I(T)}{1-\alpha} - \frac{8\tilde{I}(T)}{3-2\alpha} \right] e^{\frac{y-R}{2}} e^{-\alpha R} \left(\frac{a}{2}\right)^{1-2\alpha} \left[R + 2 \ln \frac{a}{2} \right] \quad (\text{D96})$$

Finally, we conclude that $k_y^2(a) \gg k_y^1(a)$ since $y > R$, which allows us to establish

$$\bar{k}_y(a) \sim N e^{-(\alpha+\frac{1}{2})R} e^{\frac{y}{2}} \left(\frac{a}{2}\right)^{1-2\alpha} \left[R + 2 \ln \frac{a}{2} \right] \quad (\text{D97})$$

for $y \geq R$. Equation (D64) together with Eq. (D97) establish the baseline for calculation of AUPR(a) in Subsection D 1.

Appendix E: HyperLink Embedder

The original hyperbolic geometry inference algorithm was developed in Ref. [38] and is based on maximum likelihood estimation (MLE). While the algorithm is rather slow with the overall computational complexity of $\mathcal{O}(N^3)$, it has been shown to accurately infer node coordinates in \mathbb{H}^2 leading to a number of promising applications ranging from the interdomain Internet routing [38] to understanding the growth of large-scale networks [25].

In recent years hyperbolic geometry inference has become an active area of research and a collection of alternative inference methods based has been developed by different research teams based on the MLE [49, 50], Laplacian eigenmaps [51–53] and IsoMap [53]. Even though most of these methods are characterized by relatively small computational complexity, $\mathcal{O}(N)$ - $\mathcal{O}(N^2)$, their inference accuracy has not been well explored.

At the same time, our initial experiments indicate that even small node coordinate uncertainties drastically reduce link prediction accuracy (Fig. 5). Therefore, to optimize link prediction results one needs to maximize the accuracy of node coordinate inference. To this end, we developed an enhanced MLE-based geometry inference algorithm, which we outline below.

1. General MLE formulation of hyperbolic geometry inference

Given the real network of interest with randomly removed links, we aim to find the set of node coordinates $\{\mathbf{x}_i\} \equiv \{(r_i, \theta_i)\}$, $i = 1, 2, \dots, N$, in the hyperbolic disk \mathbb{H}^2 maximizing the probability $\mathcal{L}(\{\mathbf{x}_i\}|a_{ij}, \mathcal{P}, q)$ that node coordinates take particular value in the case the network is generated as the HRG with subsequent random link removal process. Here a_{ij} is the network's observed adjacency matrix, and \mathcal{P} is the set of parameters of the HRG, $\mathcal{P} = \{\alpha, T, R\}$.

By the Bayes' rule the thought probability is given by

$$\mathcal{L}(\{\mathbf{x}_i\}|a_{ij}, \mathcal{P}, q) = \frac{\mathcal{L}(a_{ij}|\{\mathbf{x}_i\}, \mathcal{P}, q) \text{Prob}(\mathbf{x}_i)}{\mathcal{L}(a_{ij}|\mathcal{P}, q)}, \quad (\text{E1})$$

where $\mathcal{L}(a_{ij}|\{\mathbf{x}_i\}, \mathcal{P}, q)$ is the likelihood that network a_{ij} is generated as HRG with subsequent random link removal, $\text{Prob}(\mathbf{x}_i)$ is the prior probability of node coordinates generated by the HRG, and $\mathcal{L}(a_{ij}|\mathcal{P}, q)$ is the probability that the network has been generated as the HRG with random link removal.

In the following we assume the uniform prior probability

$$\text{Prob}(\mathbf{x}_i) = \frac{1}{(2\pi)^N} \prod_{i=1}^N \rho(r_i), \quad (\text{E2})$$

where $\rho(r_i)$ are given by Eq. (5). Since node pairs are connected independently, the likelihood is given by

$$\mathcal{L}(a_{ij}|\{\mathbf{x}_i\}, \mathcal{P}, q) = \prod_{i < j} [\tilde{p}(x_{ij})]^{a_{ij}} [1 - \tilde{p}(x_{ij})]^{1-a_{ij}}, \quad (\text{E3})$$

where $\tilde{p}(x_{ij})$ is the effective connection probability in the HRG generation process with subsequent random link removal:

$$\tilde{p}(x) \equiv qp(x), \quad (\text{E4})$$

where $p(x)$ is the HRG connection probability function prescribed by Eq. (6).

The MLE inference aims to find node coordinates $\hat{\mathbf{x}}_i$ maximizing the likelihood $\mathcal{L}(\{\mathbf{x}_i\}|a_{ij}, \mathcal{P}, q)$, or equivalently, its logarithm

$$\ln \mathcal{L}(\{\mathbf{x}_i\}|a_{ij}, \mathcal{P}, q) = K + \sum_{i=1}^N \ln \rho(r_i) + \sum_{i < j} [a_{ij} \ln \tilde{p}(x_{ij}) + (1 - a_{ij}) \ln (1 - \tilde{p}(x_{ij}))], \quad (\text{E5})$$

where constant K absorbs all terms independent of $\{\mathbf{x}_i\}$.

Our hyperbolic geometry inference procedure consists of three components:

1. Finite size effects and model parameter inference.
2. MLE-based inference of radial node coordinates.
3. MLE-based inference of angular node coordinates.

2. Finite size effects and model parameter inference

The HRG model has four parameters: the number of nodes N , hyperbolic disk radius R , node density parameter α and temperature T .

To infer α we first estimate the degree distribution exponent γ through the inspection of the network degree distribution $P(k)$. Node density α is related to γ through Eq. (C7).

$$\alpha = \frac{1}{2}(\gamma - 1) \quad (\text{E6})$$

The estimation of N and in R is less straightforward due to finite size effects. First, in a real network one normally can only observe nodes with non-zero degrees. In contrast, the HRG model may generate nodes of zero degree, which are accounted for in the calculation of network's average degree, \bar{k} , Eq. (C2).

Second, due to finite size effects, there is a cut of value for the smallest node radius, R_0 , affecting $\langle e^{-r/2} \rangle$ and, as a result, the observable $\bar{k}(r)$ and \bar{k} , Eqs. (C2) and (C1). Specifically, with the radius cutoff R_0

$$\langle e^{-r/2} \rangle (R_0) = \int_{R_0}^R e^{-r/2} \rho(r) dr = \langle e^{-r/2} \rangle \lambda(\alpha, R - R_0), \quad (\text{E7})$$

where $\lambda(\alpha, x)$ is the finite size correction coefficient

$$\lambda(\alpha, x) \equiv 1 - e^{-(\alpha-1/2)x}. \quad (\text{E8})$$

In the thermodynamic limit $\lambda(\alpha, (R - R_0)) \rightarrow 1$ as

$$1 - \lambda(\alpha, (R - R_0)) \sim N^{\frac{1-2\alpha}{2\alpha}} = N^{\frac{2-\gamma}{\gamma-1}}. \quad (\text{E9})$$

However, in networks with α close to $1/2$ (γ close 2) the rate of λ convergence is slow and one needs to account for non-zero R_0 .

Third, one needs to account for missing links that affect all observable properties of the HRG model. In the particular case links are missing uniformly with probability $1 - q$, the connection probability function $p(x)$ gets attenuated by the factor of q , Eq. (E4), affecting all observable network properties.

Taken together, zero degree nodes, minimum radius cutoff and missing links affect observable network properties as follows:

$$\tilde{N} = N(1 - P(0)), \quad (\text{E10})$$

$$\tilde{k} = \frac{q [\lambda(\alpha, R - R_0)]^2}{1 - P(0)} \bar{k}, \quad (\text{E11})$$

$$\tilde{k}_{\max} \approx q \lambda(\alpha, R - R_0) \bar{k} \frac{e^{-R_0}}{\langle e^{-r/2} \rangle}, \quad (\text{E12})$$

where \tilde{k}_{\max} is the maximum degree observed in the network and $P(0)$ is the fraction of zero degree nodes in the network. The latter can be estimated by averaging the conditional degree distribution $P(k = 0|r)$ in Eq. (C5) over possible r values:

$$P(0) = 2\alpha\tau^{2\alpha}\Gamma[-\alpha, \tau], \quad (\text{E13})$$

$$\tau \equiv q [\lambda(\alpha, R - R_0)] \bar{k} \frac{e^{-R/2}}{\langle e^{-r/2} \rangle}, \quad (\text{E14})$$

where $\Gamma[s, x]$ is the upper incomplete gamma function.

Equations. (E10), (E11), (E12), (E13) and (E14) allow one to infer the HRG parameters R_0 , R , N as well as resulting \bar{k} , and $P(0)$ by measuring observables \tilde{N} , \tilde{k} , and \tilde{k}_{\max} .

The caveat here is that parameter estimation presumes the knowledge of the missing link probability $1 - q$. While this information is available in our synthetic experiments, it may not be available in real networks. In case the fraction of missing links is small, one can assume that $q = 1$. The most general case of substantially incomplete networks where $q \ll 1$ is beyond the scope of this work and will be studied elsewhere.

Finally, the temperature parameter T needs to be estimated numerically by finding the solution of

$$\bar{c}(T) = c_0, \quad (\text{E15})$$

where c_0 is the average clustering coefficient of the network of interest and $\bar{c}(T)$ is the average clustering coefficient of the HRG model generated with temperature T . We utilize this approach to infer T of real networks in Section IV B, while in experiments with HRG models we use actual T values.

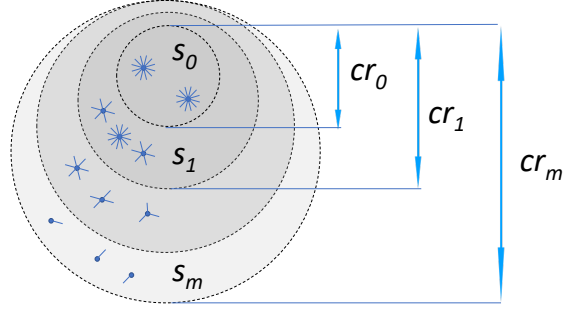


FIG. 15: Layered network structure for MLE inference. Nodes are sorted in the decreasing order of their degree and placed into logarithmically-sized layers. The outer layer contains only $k = 1$ nodes.

3. MLE-based inference of radial node coordinates

To infer radial node coordinates we extremize the logarithm of the likelihood function,

$$\frac{\partial}{\partial r_\ell} \ln \mathcal{L}(\{\mathbf{x}_i\} | a_{ij}, \mathcal{P}, q) = 0, \quad (\text{E16})$$

obtaining

$$2\alpha T \coth(\alpha r_\ell) + \sum_j \left[\frac{1 - p(x_{\ell j})}{1 - qp(x_{\ell j})} (a_{\ell,j} - qp(x_{\ell,j})) \right] \frac{\partial x_{\ell j}}{\partial r_\ell} = 0. \quad (\text{E17})$$

In the case of sufficiently large r values $\coth(\alpha r_\ell) \approx 1$. Further, one can approximate $x_{\ell j}$ as

$$x_{\ell j} \approx r_\ell + r_j + \ln \sin \theta_{\ell j} / 2, \quad (\text{E18})$$

resulting in $\frac{\partial x_{\ell j}}{\partial r_\ell} \approx 1$. Taken together, these approximations allow us to simplify Eq.(E17) as

$$2\alpha T + \sum_j a_{\ell,j} - q \sum_j p(x_{\ell,j}) = 0 \quad (\text{E19})$$

for $1 - q \ll 1$. Note that the first summation in Eq. (E19) is the degree of node ℓ , $\sum_j a_{\ell,j} = k_\ell$, while the second summation is the expected degree of node with r_ℓ , $\tilde{k}(r_\ell) = q \sum_j p(x_{\ell,j})$. As a result, the value of \hat{r}_ℓ extremizing the likelihood is given by

$$\tilde{k}(\hat{r}_\ell) = k_\ell + 2\alpha T, \quad (\text{E20})$$

where $\tilde{k}(r)$ is the observable expected degree of node with radial coordinate r . Since the latter is given by

$$\tilde{k}(r) = q\lambda(\alpha, R - R_0) \bar{k} \frac{e^{-r/2}}{\langle e^{-r/2} \rangle}, \quad (\text{E21})$$

one can estimate \hat{r}_ℓ as

$$\hat{r}_\ell = 2 \ln \left[\frac{q\lambda(\alpha, R - R_0) \bar{k}}{(k_\ell + 2\alpha T) \langle e^{-r/2} \rangle} \right]. \quad (\text{E22})$$

4. MLE inference of angular node coordinates

To infer angular node coordinates one needs to maximize the likelihood $\ln \mathcal{L}(\{\mathbf{x}_i\} | a_{ij}, \mathcal{P}, q)$ in Eq. (E5) with respect to angular coordinates $\{\theta_i\}$, given the MLE values for radial coordinates $\{\hat{r}_i\}$. Since the maximization of

Algorithm 1 Angular MLE Inference

```

organize network nodes into layers  $\{s_i\}$  and cores  $\{cr_i\}$ ,  $i = 0, 1, \dots, m$ .
define the sequence of subgraphs  $\{G_i\}$  spanned by nodes in  $\{cr_i\}$ .
for iter = 0 to max_iter do
  for  $\ell = 0$  to  $\lfloor m/2 \rfloor$  (first half) do
    assign random angle values,  $\theta_i \sim U[0, 2\pi]$ , to nodes in  $s_\ell$ .
    Other nodes in  $G_\ell$  retain their previous angular positions.
     $a(\ell) \leftarrow \frac{\pi}{4} \left(1 - \frac{\ell}{m}\right) + a_0$ .
    for all nodes  $i$  in  $G_\ell$  do
       $X_i \sim U\left(-\frac{\pi}{2}, \frac{\pi}{2}\right)$ .
       $\hat{\theta}_i \leftarrow \hat{\theta}_i + a(\ell)X_i$ .
    end for
    repeat
      for all nodes  $i$  in  $G_\ell$  do
         $\hat{\theta}_i \leftarrow \operatorname{argmax} \ln \mathcal{L}[G_\ell]_i$ , see Alg. 2.
      end for
    until  $(\max_{i \in G_\ell} \Delta \hat{\theta}_i < \epsilon)$  or  $(\# \text{ rounds} > \text{max\_rounds})$ 
  end for
  compute resulting log-likelihood  $\ln \mathcal{L}[G_{\lfloor m/2 \rfloor}]$  value and save corresponding  $\{\theta_i\}$  values.
end for
continue with  $\{\theta_i\}$  values corresponding to the largest  $\ln \mathcal{L}[G_{\lfloor m/2 \rfloor}]$ .
for  $\ell = \lfloor m/2 \rfloor + 1$  to  $m$  (second half) do
  assign random  $\{\theta_i\}$  values to nodes in  $s_\ell$ . Other nodes in  $G_\ell$  retain their previous angular positions.
  repeat
    for all nodes  $i$  in  $G_\ell$  do
       $\hat{\theta}_i \leftarrow \operatorname{argmax} \ln \mathcal{L}[G_\ell]_i$ , see Alg. 2.
    end for
  until  $(\max_{i \in G_\ell} \Delta \hat{\theta}_i < \epsilon)$  or  $(\# \text{ rounds} > \text{max\_rounds})$ 
   $a(\ell) \leftarrow \frac{\pi}{4} \left(1 - \frac{\ell}{m}\right) + a_0$ .
  for all nodes  $i$  in  $G_\ell$  do
     $X_i \sim U\left(-\frac{\pi}{2}, \frac{\pi}{2}\right)$ .
     $\hat{\theta}_i \leftarrow \hat{\theta}_i + a(\ell)X_i$ .
  end for
end for

```

$\ln \mathcal{L}(\{\mathbf{x}_i\}|a_{ij}, \mathcal{P}, q)$ with respect to $\{\theta_i\}$ cannot be performed analytically, we have to rely on numerical approximations. To this end, we developed an MLE-based algorithm optimized for the linked prediction problem.

Conceptually, our algorithm is similar to the one developed in Ref. [38] but has several important differences.

Following the exposition of Ref. [38], we make two observations based on the link independence in HRG. First, angular coordinates of any node subset \mathbb{S} can be inferred independently (albeit, with lower accuracy) based only on the partial information contained in the graph $G_{\mathbb{S}}$ formed by these nodes. In other words, the inference of angular coordinates in \mathbb{S} is possible by maximizing \mathbb{S} -specific log-likelihood:

$$\ln \mathcal{L}[G_{\mathbb{S}}] = \frac{1}{2} \sum_{\{i,j\} \in G_{\mathbb{S}}} [a_{ij} \ln \tilde{p}(x_{ij}) + (1 - a_{ij}) \ln (1 - \tilde{p}(x_{ij}))]. \quad (\text{E23})$$

Second, any log-likelihood $\mathcal{L}[G_{\mathbb{S}}]$ can be represented as a sum of local contributions $\mathcal{L}[G_{\mathbb{S}}]_i$:

$$\ln \mathcal{L}[G_{\mathbb{S}}] = \frac{1}{2} \sum_i \ln \mathcal{L}[G_{\mathbb{S}}]_i, \quad (\text{E24})$$

where

$$\ln \mathcal{L}[G_{\mathbb{S}}]_i = \sum_{j \neq i \in G_{\mathbb{S}}} [a_{ij} \ln \tilde{p}(x_{ij}) + (1 - a_{ij}) \ln (1 - \tilde{p}(x_{ij}))]. \quad (\text{E25})$$

Since the log likelihood profile $\ln \mathcal{L}(\{\mathbf{x}_i\}|a_{ij}, \mathcal{P}, q)$ is non-convex with abundant local maxima, we do not intend to find its global maximum by optimizing all angles at once. Instead, we proceed in a nested fashion by organizing network nodes into logarithmically-sized layers with nodes of larger degree belonging to inner layers. To this end, we

define the set \mathbb{C} of all nodes with degrees $k > 1$. We then rank all nodes in \mathbb{C} in the decreasing order of their degree value, and split the resulting node list into m layers with logarithmically growing sizes s_i , $i = 0, \dots, m-1$:

$$s_{i+1} = \lfloor w \times s_i \rfloor, \quad (\text{E26})$$

$$w = [N(k > 1)]^{1/m}, \quad (\text{E27})$$

where $N(k > 1)$ is the number of nodes with degree $k > 1$, and $s_0 \ll N$. Unless otherwise noted, we set $s_0 = 20$. Finally, all $k = 1$ nodes are assigned to the outer layer s_m .

Complementary to layers $\{s_i\}$, we also define self-enclosed cores $\{cr_i\}$, $i = 0, \dots, m$, such that core cr_i contains all layer with indices $j \leq i$, $cr_i = \bigcup_{j=0}^i s_j$, as well as the sequence of nested subgraphs $\{G_i\}$, $i = 0, \dots, m$, spanned by the nodes in corresponding cores, see Fig. 15.

We start by inferring node angular coordinates $i \in cr_0$ by maximizing G_0 -specific likelihood $\ln \mathcal{L}[G_0]$. We then utilize the inferred angles $\{\theta_i\} \in cr_0$ as initial approximation to maximize $\ln \mathcal{L}[G_1]$. We continue the angular coordinate inference procedure in the nested fashion to find angular values maximizing $\ln \mathcal{L}[G_m]$:

$$\ln \mathcal{L}[G_0] \rightarrow \ln \mathcal{L}[G_1] \rightarrow \dots \rightarrow \ln \mathcal{L}[G_m]. \quad (\text{E28})$$

We maximize each log-likelihood $\ln \mathcal{L}[G_\ell]$ iteratively by visiting G_ℓ nodes in rounds. At each round every node i in G_ℓ is visited once and placed at $\hat{\theta}_i$ maximizing its local log-likelihood $\mathcal{L}[G_\ell]_i$ with respect to the current angular values of other nodes in G_ℓ . The procedure is continued until we arrive at the stable angular configuration:

$$\max_{i \in G_\ell} \Delta \hat{\theta}_i < \epsilon, \quad (\text{E29})$$

where $0 < \epsilon \ll 1$ is the precision parameter, and $\Delta \hat{\theta}_i$ is the angular difference between angular positions of node i in two consecutive rounds. In our experiments we set $\epsilon = 10^{-4}$ radians.

The required total number of all-node visit rounds is typically small, of the order of the network average degree. In certain circumstances, e.g., in the case of the global $\ln \mathcal{L}[G_\ell]$ maximum close to the second largest maximum, the procedure may require a large number of rounds to converge. To avoid these scenarios we limit the maximum number of rounds to 10 per G_ℓ .

Our experiments indicate that the resulting HyperLink link prediction accuracy is highly sensitive to the correct placement of highest degree nodes. Thus, to further improve angular inference of the most connected nodes, we split the procedure into two parts, $\ell = 0, 1, \dots, \lfloor m/2 \rfloor$ and $\ell = \lfloor m/2 \rfloor + 1, \dots, m$, respectively. The first part is repeated independently for $\text{max_iter} = 20$ times, starting from different initial angle values. For each repetition the resulting $\ln \mathcal{L}[G_{\lfloor m/2 \rfloor}]$ value is computed. The second part is carried out only once using $\{\theta_i\}$ values corresponding to the iteration with largest $\ln \mathcal{L}[G_{\lfloor m/2 \rfloor}]$ value. Since $\ell = 0, 1, \dots, \lfloor m/2 \rfloor$ cores are significantly smaller than $\ell = \lfloor m/2 \rfloor + 1, \dots, m/2$ cores, the first part is carried out much faster than the second, despite the large number of repetitions.

After each round ℓ we perturb the angular coordinates $\hat{\theta}_i$, $i \in cr_\ell$, by adding random noise

$$\hat{\theta}_i \leftarrow \hat{\theta}_i + a(\ell)X_i, \quad (\text{E30})$$

$$X_i \sim U\left(-\frac{\pi}{2}, \frac{\pi}{2}\right), \quad (\text{E31})$$

with amplitude $a(\ell)$, which we decrease linearly as $a(\ell) = \frac{\pi}{4}\left(1 - \frac{\ell}{m}\right) + a_0$. These coordinate perturbations allow us to avoid getting trapped in local maxima of the log-likelihood function and to arrive to the optimal angles $\{\theta_i\}$ faster. We also stress the importance of the non-zero residual noise amplitude of a_0 . In the final $\ell = m$ stage residual noise allows to effectively "repel" $k = 1$ nodes connected to the same node. Without residual noise at the $\ell = m$ step, all $k = 1$ nodes connected to the same node are likely to be placed very close to each other and their common neighbor. As a result, pairs of these $k = 1$ nodes will be ranked as the most likely candidates for link prediction, and will adversely affect the HyperLink accuracy. Our experiments indicate that the HyperLink accuracy is not sensitive to specific a_0 values, as long as $a_0 \in [10^{-6}, 10^{-3}]$. In all our experiments we set $a_0 = 10^{-4}$ radians. The angular inference procedure is summarized in Alg. 1.

Having sketched the angular inference procedure, we now focus on the individual node placement subroutine. We determine $\hat{\theta}_i$ for each node by maximizing the corresponding local log-likelihood $\ln \mathcal{L}[G_\ell]_i$. To this end, we split the angular space $[-\pi, \pi]$ evenly into $\mathcal{O}(N_\ell)$ regions, where N_ℓ is the number of nodes in G_ℓ . By placing node i into each of these regions we then identify $\hat{\theta}_i$ maximizing its local likelihood. Since $\ln \mathcal{L}[G_\ell]_i$ calculation takes $\mathcal{O}(N_\ell)$ steps for each θ_i value, it takes $\mathcal{O}(N_\ell^2)$ steps to execute each round ℓ . As a result, the overall running-time complexity for m layers, $\mathcal{O}(mN^3)$, is prohibitive for large networks.

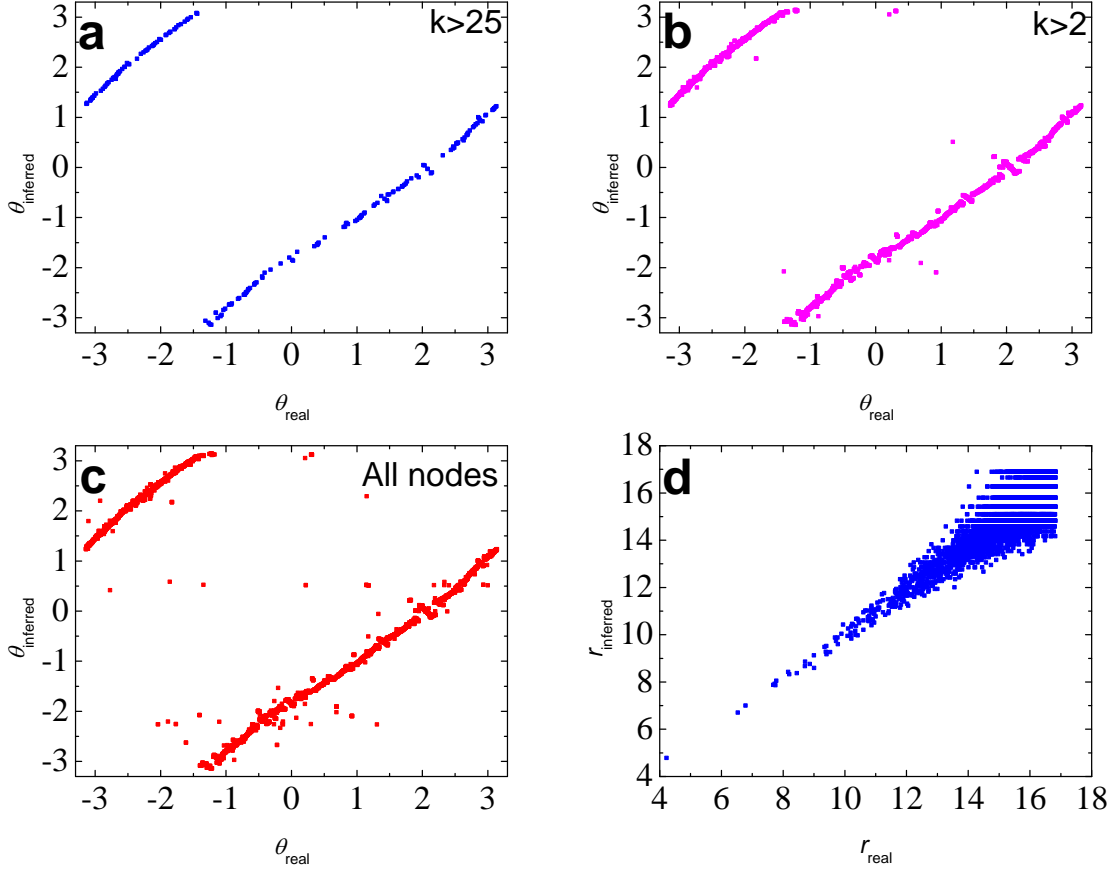


FIG. 16: **Testing the hyperbolic geometry inference algorithm.** Here we plot inferred vs original node coordinates for the HRG graph that we map to the hyperbolic space. All plots correspond to the same HRG network of $N = 5,000$, $\langle k \rangle = 10$, $T = 0.5$, and $\gamma = 2.5$. Panels **a** and **b** display angular coordinates for nodes with degrees $k > 25$ and $k > 2$, respectively. Panel **c** displays angular coordinates of all nodes. Panel **d** displays radial coordinates of all nodes in the graph.

To reduce the running time complexity to $\mathcal{O}(m\langle k \rangle N^2)$, where $\langle k \rangle$ is the average degree of the entire network we utilize the following approximation, first offered in Ref. [38]. For each node we first obtain the rough estimate of $\hat{\theta}_i$ by taking into account only its neighboring nodes in G_ℓ . To this end we find the nearly-optimal placement $\tilde{\theta}_i$ by maximizing

$$\ln \tilde{\mathcal{L}}[G_S]_i = \sum_{j \neq i \in G_S} a_{ij} \ln \tilde{p}(x_{ij}). \quad (\text{E32})$$

Since the summation in Eq. (E32) goes only through node i neighbors, it now takes $\mathcal{O}(k_i N)$ steps to find $\tilde{\theta}_i$. Having obtained the initial approximation, we then look for the optimal angle $\hat{\theta}_i$ in the neighborhood of $\tilde{\theta}_i$ maximizing the full local likelihood $\ln \mathcal{L}[G_S]_i$, which takes $\mathcal{O}(LN)$ steps, where L is the neighborhood centered at $\tilde{\theta}_i$. Specifically, we search for $\hat{\theta}_i$ within $L = 300 \frac{N_\ell}{N}$ regions on both sides of $\tilde{\theta}_i$, which takes $\mathcal{O}\left(\frac{N_\ell^2}{N}\right)$ steps, leading to the overall running time complexity of $\mathcal{O}(m\langle k \rangle N^2)$ steps. The individual node placement subroutine is summarized in Alg. 2.

To validate the hyperbolic geometry inference algorithm we compare inferred coordinates in the HRG model network to its true coordinates. Parameters of the HRG are taken to be $N = 5,000$, $\langle k \rangle = 10$, $T = 0.5$, and $\gamma = 2.5$. As seen from Figs. 16 **a-c**, the accuracy of the angular coordinate inference does not decline significantly for small degree nodes. This is the case, mainly, due to the nested inference with inference cores cr_i covering all network nodes, in contrast to the original algorithm of Ref. [38], where cores only cover the most connected nodes.

As seen from Fig. 16 **d**, Eq. (E22) allows for accurate inference of small radial coordinates. At the same time, radial coordinates inference is less accurate for large radial coordinates. To explain this observation we recall that the key assumption in Eq. (E22) is that the node degree, in the HRG is fully determined by its radial coordinate. In other words, we assume that possible node degree values are narrowly distributed around its expected value, which is

Algorithm 2 Individual node placement subroutine

split the angular space $[-\pi, \pi]$ evenly into $\mathcal{O}(N_\ell)$ regions.

for each region r in $[-\pi, \pi]$ **do**

 sample $\theta_i(r)$ uniformly at random from region r .

 compute $\ln \tilde{\mathcal{L}}[G_\ell]_i$ for $\theta_i(r)$, as defined in Eq. (E32).

end for

$\hat{\theta}_i \leftarrow \operatorname{argmax}_{r \in [-\pi, \pi]} \ln \tilde{\mathcal{L}}[G_\ell]_i$

for each region r in $[\|\hat{\theta}_i - L\|, \|\hat{\theta}_i + L\|]$ **do**

 sample $\theta_i(r)$ uniformly at random from region r .

 compute $\ln \mathcal{L}[G_\ell]_i$ for $\theta_i(r)$.

end for

Identify \hat{r} maximizing $\ln \mathcal{L}[G_\ell]_i$. $\hat{\theta}_i \leftarrow \theta_i(\hat{r})$

$\hat{\theta}_i \leftarrow \operatorname{argmax}_{r \in [\|\hat{\theta}_i - L\|, \|\hat{\theta}_i + L\|]} \ln \mathcal{L}[G_\ell]_i$

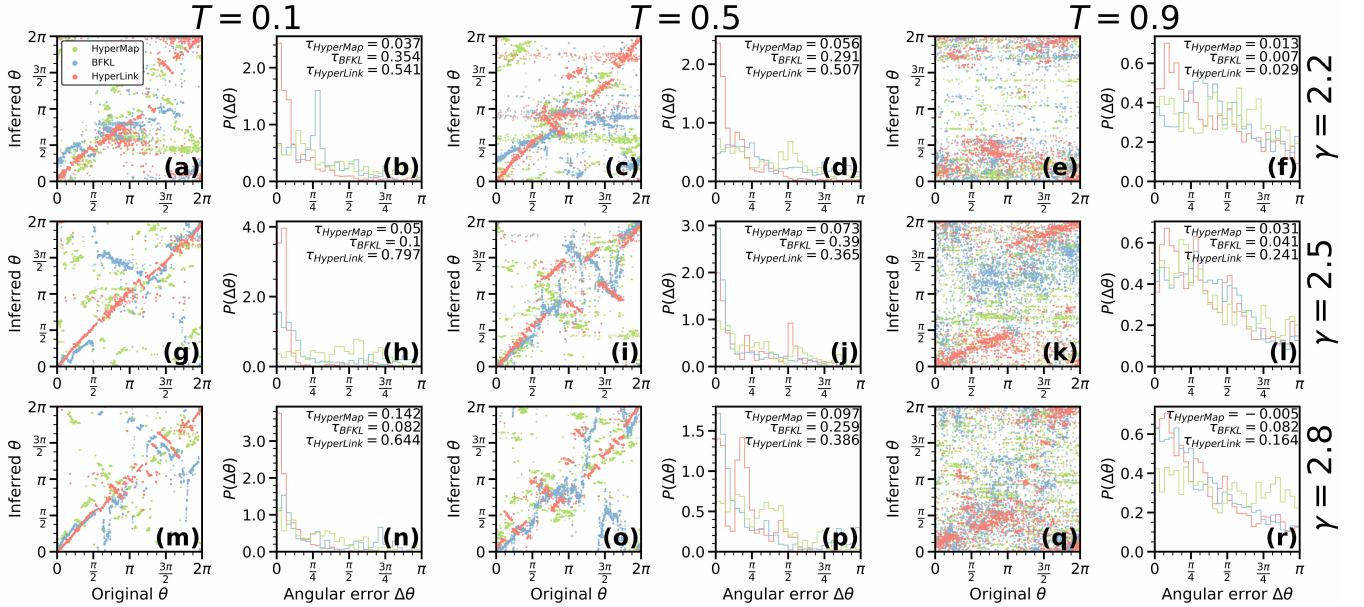


FIG. 17: HyperLink Embedder accuracy compared to other embedding algorithms. HRGs are embedded to the hyperbolic disk by (red) HyperLink Embedder, (blue) the algorithm by Bläsius et al. [49] (BFKL), and (green) the HyperMap [34] algorithm. All comparisons correspond to HRGs consisting of $N = 5,000$ nodes, $\bar{k} = 10$, $1 - q = 0.5$ missing links and various T and γ parameters. Panels are arranged according to T and γ parameters. Panels **a, c, e, g, i, k, m, o, q** correspond to the scatter plots displaying inferred angular coordinates as a function of true angular coordinates. To quantify the embedding accuracy, we plot the distributions of embedding errors, $P(\Delta\theta)$, where $\Delta\theta \equiv \pi - |\pi - |\theta_{\text{inferred}} - \theta_{\text{original}}||$ in panels **b, d, f, h, j, l, n, p, r**, respectively. To quantify the association between the inferred and the original angular coordinates for each embedding we employ the U-statistic $\tau \in [-1, 1]$, Ref [61]. The U-statistic τ quantifies the correlation between the ordering of the inferred and original and angular coordinates and ranges from $\tau = 1$, in the case the two orderings are the same, to $\tau = -1$ in the case the two orderings are inverted with respect to one another. The U-statistic τ is invariant under global shifts of the inferred coordinates. Our results indicate that the HyperLink accuracy is higher than that of the considered two algorithms in all cases, with the only exception of the $T = 0.5$, $\gamma = 2.5$ case, where BFKL is slightly better.

given by Eq. (E22). This is indeed the case since node degree are distributed according to the Poisson distribution, Eq. (C5). The coefficient of variation of the Poisson distribution, however, is large for small mean values. This leads to significant variation in node degree values in the case of nodes with large radial coordinates, making Eq. (E22) inaccurate.

The HyperLink Embedder allows for accurate node coordinate inference even in substantially incomplete networks in contrast to other mapping methods, e.g., HyperMap [33] and the algorithm by Bläsius et al. [49], which become less accurate in the case of large T values, Fig. 17.

As evidenced by Fig. 16 and, indirectly, by our link prediction results in Sections III and IV, our hyperbolic inference algorithm is sufficiently accurate for the prediction of missing links on both synthetic and real networks. At the same time, the algorithm does have limitations. First, it is designed to map networks with links removed uniformly at random. The link presence rate q is the required parameter of the algorithm. In cases when the fraction of missing

links is unknown, q needs to be estimated and this may lead to less accurate mapping. The second limitation is the algorithm's running time complexity of $\mathcal{O}(N^2)$ restricting its utility to networks of smaller size. Finally, the third limitation is the analytic estimation of radial coordinates which is not accurate for small degree nodes. Addressing these limitations is the subject of the future work that is expected to further improve the accuracy and the utility of link prediction with hyperbolic geometry.

-
- [1] W. Peng, X. Baowen, W. Yurong, and Z. Xiaoyu, *Link prediction in social networks : the state-of-the-art*, *Sci. China Inf. Sci.* **58**, 011101 (2015).
 - [2] L. Lü and T. Zhou, *Link prediction in complex networks: A survey*, *Phys. A Stat. Mech. its Appl.* **390**, 1150 (2011).
 - [3] A. K. Menon and C. Elkan, in *ECML PKDD 2011*, Vol. 6912 (2011) pp. 437–452.
 - [4] T. P. Peixoto, *Reconstructing Networks with Unknown and Heterogeneous Errors*, *Phys. Rev. X* **8**, 041011 (2018).
 - [5] D. J. Marchette and C. E. Priebe, *Predicting unobserved links in incompletely observed networks*, *Comput. Stat. Data Anal.* **52**, 1373 (2008).
 - [6] M. Kim and J. Leskovec, *The Network completion problem: Inferring missing nodes and edges in networks*, *SIAM Int. Conf. Data Min.*, 47 (2011).
 - [7] L. A. Adamic and E. Adar, *Friends and neighbors on the Web*, *Soc. Networks* **25**, 211 (2003).
 - [8] M. E. J. Newman and A. Clauset, *Structure and inference in annotated networks*, *Nat. Commun.* **7**, 1 (2016).
 - [9] C. von Mering, R. Krause, B. Snel, M. Cornell, S. G. Oliver, S. Fields, and P. Bork, *Comparative assessment of large-scale data sets of proteinprotein interactions*, *Nature* **217**, 399 (2002).
 - [10] H. Yu, P. Braun, and M. A. Yildirim et al., *High-quality binary protein interaction map of the yeast interactome network*, *Science* **322**, 104 (2008).
 - [11] I. A. Kovács, K. Luck, and K. Spirohn et al., *Network-based prediction of protein interactions*, *bioRxiv*, 275529 (2018), [arXiv:275529](https://arxiv.org/abs/275529).
 - [12] T. Zhou, J. Ren, M. Medo, and Y.-C. Zhang, *Bipartite network projection and personal recommendation*, *Phys. Rev. E* **76**, 046115 (2007).
 - [13] L. Lü, M. Medo, C. H. Yeung, Y.-C. Zhang, Z.-K. Zhang, and T. Zhou, *Recommender systems*, *Phys. Rep.* **519**, 1 (2012).
 - [14] J. Bobadilla, F. Ortega, A. Hernando, and A. Gutiérrez, *Recommender systems survey*, *Knowledge-Based Syst.* **46**, 109 (2013).
 - [15] J. B. Schafer, J. Konstan, and J. Riedl, in *Proc. 1st ACM Conf. Electron. Commer.* (ACM, 1999) pp. 158–166.
 - [16] E. N. Gilbert, *Random plane networks*, *J. Soc. Ind. Appl. Math.* **9**, 533 (1961).
 - [17] D. D. McFarland and D. J. Brown, *Social distance as a metric: a systematic introduction to smallest space analysis*, *Bond. Plur. Form Subst. Urban Soc. Networks* **6**, 213 (1973).
 - [18] M. McPherson, L. Smith-Lovin, and J. M. Cook, *Birds of a feather: Homophily in social networks*, *Annu. Rev. Sociol.* **27**, 415 (2001).
 - [19] D. Krioukov, F. Papadopoulos, M. Kitsak, A. Vahdat, and M. Boguñá, *Hyperbolic geometry of complex networks*, *Phys. Rev. E* **82**, 036106 (2010).
 - [20] M. E. J. Newman and T. P. Peixoto, *Generalized communities in networks*, *Phys. Rev. Lett.* **115**, 088701 (2015).
 - [21] A. Brew, *A latent space mapping for link prediction*, *Neural Inf. Process.*, 1 (1998).
 - [22] L. Zhu, D. Guo, J. Yin, G. V. Steeg, and A. Galstyan, *Scalable temporal latent space inference for link prediction in dynamic social networks*, *IEEE Trans. Knowl. Data Eng.* (2016).
 - [23] G. García-Pérez, R. Aliakbarisani, A. Ghasemi, and M. Á. Serrano, *Predictability of missing links in complex networks*, (2019), [arXiv:1902.00035](https://arxiv.org/abs/1902.00035).
 - [24] M. Serrano, D. Krioukov, and M. Boguñá, *Self-similarity of complex networks and hidden metric spaces*, *Phys. Rev. Lett.* **100**, 078701 (2008).
 - [25] F. Papadopoulos, M. Kitsak, M. Á. Serrano, M. Boguñá, and D. Krioukov, *Popularity versus similarity in growing networks*, *Nature* **489**, 537 (2012).
 - [26] K. Zuev, M. Boguñá, G. Bianconi, and D. Krioukov, *Emergence of soft communities from geometric preferential attachment*, *Sci. Rep.* **5**, 9421 (2015).
 - [27] E. Lazega, S. Wasserman, and K. Faust, *Social Network Analysis: Methods and Applications*, *Rev. Française Sociol.* (2006).
 - [28] M. Newman, *Networks: An Introduction* (Oxford University Press, 2010).
 - [29] A.-L. Barabasi and M. Posfai, *Network science* (Cambridge University Press, 2016) p. 456.
 - [30] P. van der Hoorn, G. Lippner, and D. Krioukov, *Sparse Maximum-Entropy Random Graphs with a Given Power-Law Degree Distribution*, *J. Stat. Phys.* **173**, 806 (2018).
 - [31] D. Krioukov, *Clustering Implies Geometry in Networks*, *Phys. Rev. Lett.* **116** (2016).
 - [32] M. Á. Serrano, M. Boguñá, and F. Sagués, *Uncovering the hidden geometry behind metabolic networks*, *Mol. Biosyst.* **8**, 843 (2012).
 - [33] F. Papadopoulos, C. Psomas, and D. Krioukov, *Network mapping by replaying hyperbolic growth*, *IEEE/ACM Trans. Netw.* **23**, 198 (2015).
 - [34] F. Papadopoulos, R. Aldecoa, and D. Krioukov, *Network geometry inference using common neighbors*, *Phys. Rev. E* **92**, 022807 (2015).
 - [35] A. Muscoloni and C. V. Cannistraci, *Leveraging the nonuniform PSO network model as a benchmark for performance evaluation in community detection and link prediction*, *New J. Phys.* **20** (2018).
 - [36] A. Muscoloni and C. V. Cannistraci, *Minimum curvilinear automata with similarity attachment for network embedding and link prediction in the hyperbolic space*, (2018), [arXiv:1802.01183](https://arxiv.org/abs/1802.01183).
 - [37] D. Krioukov, F. Papadopoulos, A. Vahdat, and M. Boguñá, *Curvature and temperature of complex net-*

- works, *Phys. Rev. E* **80**, 35101 (2009).
- [38] M. Boguñá, F. Papadopoulos, and D. Krioukov, *Sustaining the Internet with hyperbolic mapping*, *Nat. Commun.* **1**, 62 (2010).
 - [39] M. Kitsak, F. Papadopoulos, and D. Krioukov, *Latent geometry of bipartite networks*, *Phys. Rev. E* **95**, 032309 (2017).
 - [40] R. Aldecoa, C. Orsini, and D. Krioukov, *Hyperbolic graph generator*, *Comput. Phys. Commun.* **196**, 492 (2015).
 - [41] G. García-Pérez, M. Boguñá, and M. Á. Serrano, *Multiscale unfolding of real networks by geometric renormalization*, *Nat. Phys.* , 1 (2018).
 - [42] A. Muscoloni and C. V. Cannistraci, *A nonuniform popularity-similarity optimization (nPSO) model to efficiently generate realistic complex networks with communities*, *New J. Phys.* **20**, 052002 (2018).
 - [43] J. Davis and M. Goadrich, in *Proc. 23rd Int. Conf. Mach. Learn. - ICML '06* (2006) pp. 233–240.
 - [44] G. Alanis-Lobato and M. A. Andrade-Navarro, *Distance distribution between complex network nodes in hyperbolic space*, *Complex Syst.* **25**, 223 (2016).
 - [45] *University of Oregon Route Views Project* , <http://www.routeviews.org/routeviews/>.
 - [46] H. Ma and A.-P. Zeng, *Reconstruction of metabolic networks from genome data and analysis of their global structure for various organisms*, *Bioinformatics* **19**, 270 (2003).
 - [47] *The Open PGP Alliance*, <http://www.openpgp.org/>.
 - [48] L. Lü, L. Pan, T. Zhou, Y.-C. Zhang, and H. E. Stanley, *Toward link predictability of complex networks*, *Proc. Natl. Acad. Sci.* **112**, 2325 (2015).
 - [49] T. Bläsius, T. Friedrich, A. Krohmer, and S. Laue, in *24th Annu. Eur. Symp. Algorithms (ESA 2016)*, Vol. 57 (2016) pp. 16:1—16:18.
 - [50] Z. Wang, Y. Wu, Q. Li, F. Jin, and W. Xiong, *Link prediction based on hyperbolic mapping with community structure for complex networks*, *Phys. A Stat. Mech. its Appl.* **450**, 609 (2016).
 - [51] G. Alanis-Lobato, P. Mier, and M. A. Andrade-Navarro, *Efficient embedding of complex networks to hyperbolic space via their Laplacian*, *Sci. Rep.* **6**, 30108 (2016).
 - [52] G. Alanis-Lobato, P. Mier, and M. A. Andrade-Navarro, *Manifold learning and maximum likelihood estimation for hyperbolic network embedding*, *Appl. Netw. Sci.* **1**, 10 (2016).
 - [53] A. Muscoloni, J. M. Thomas, S. Ciucci, G. Bianconi, and C. V. Cannistraci, *Machine learning meets complex networks via coalescent embedding in the hyperbolic space*, *Nat. Commun.* **8** (2017).
 - [54] *OpenPGP web of trust database*, <http://www.lysator.liu.se/~jc/wotsap/wots2/>.
 - [55] I. Voitalov, P. van der Hoorn, R. van der Hofstad, and D. Krioukov, *Scale-free Networks Well Done*, (2018), [arXiv:1811.02071](https://arxiv.org/abs/1811.02071) .
 - [56] D. Liben-Nowell and J. Kleinberg, *The Link Prediction Problem for Social Networks*, *Proc. Twelfth Annu. ACM Int. Conf. Inf. Knowl. Manag.* , 556 (2003).
 - [57] T. Zhou, L. Lü, and Y. C. Zhang, *Predicting missing links via local information*, *Eur. Phys. J. B* **71**, 623 (2009).
 - [58] C. V. Cannistraci, G. Alanis-Lobato, and T. Ravasi, *From link-prediction in brain connectomes and protein interactomes to the local-community-paradigm in complex networks*, *Sci. Rep.* **3**, 1613 (2013).
 - [59] P. Jaccard, *Étude comparative de la distribution florale dans une portion des Alpes et des Jura*, *Bull. del la Société Vaudoise des Sci. Nat.* **37**, 547 (1901).
 - [60] M. Boguñá and R. Pastor-Satorras, *Class of correlated random networks with hidden variables*, *Phys. Rev. E* **68**, 036112 (2003).
 - [61] N. Fisher and A. Lee, *Nonparametric measures of angular-angular association*, *Biometrika* **69**, 315 (1982).